

Galactic Winds in Cosmological Simulations of the Circumgalactic Medium

Paramita Barai^{1*}, Matteo Viel^{1,2}, Stefano Borgani^{3,1,2}, Edoardo Tescari^{4,5}, Luca Tornatore³, Klaus Dolag^{6,7}, Madhura Killeidar^{3,1}, Pierluigi Monaco^{3,1}, Valentina D’Odorico¹, Stefano Cristiani^{1,2}

¹ INAF - Osservatorio Astronomico di Trieste, Via G.B. Tiepolo 11, I-34143 Trieste, Italy

² INFN / National Institute for Nuclear Physics, Via Valerio 2, I-34127 Trieste, Italy

³ Dipartimento di Fisica dell’Università di Trieste, Sezione di Astronomia, Via Tiepolo 11, I-34131 Trieste, Italy

⁴ School of Physics, University of Melbourne, Parkville, VIC 3010, Australia

⁵ ARC Centre of Excellence for All-Sky Astrophysics (CAASTRO)

⁶ Universitätssternwarte München, München, Germany

⁷ Max-Planck-Institut für Astrophysik, Garching, Germany

1 September 2018

ABSTRACT

We explore new observationally-constrained sub-resolution models of galactic outflows and investigate their impact on the circumgalactic medium (CGM) in the redshift range $z = 2 - 4$. We perform cosmological hydrodynamic simulations, including star formation, chemical enrichment, and four cases of SNe-driven outflows: no wind (NW), an energy-driven constant velocity wind (CW), a radially varying wind (RVWa) where the outflow velocity has a positive correlation with galactocentric distance (r), and a RVW with additional dependence on halo mass (RVWb). Overall, we find that the outflows expel metal-enriched gas away from galaxies, significantly quench the star formation, reduce the central galactic metallicity and enrich the CGM. At $z = 2$, the radial profiles of gas properties around galaxy centers are most sensitive to the choice of the wind model for halo masses in the range $(10^9 - 10^{11})M_{\odot}$.

We infer that outflows in the RVWb model are least effective, with results similar to the NW case, except that the CGM is enriched more. Moreover, we find that the models CW and RVWa are similar, both showing the impact of effective winds, with the following notable differences. RVWa causes a greater suppression of star formation rate at $z \leq 5$, and has a higher fraction of low-density ($\delta < 10$), warm-hot ($10^4 - 10^6$ K) gas than in CW. Outflows in CW produce a higher and earlier enrichment of some IGM phases than in RVWa. By visual inspection, we note that the RVWa model shows galactic disks more pronounced than all the other wind models. We predict that some observational diagnostics are more promising to distinguish between different outflow driving mechanisms in galaxies: Z_C of the CGM gas at $r \sim (30 - 300)h^{-1}$ kpc comoving, and CIV fraction of the inner gas at $r < (4 - 5)h^{-1}$ kpc comoving.

Key words: Cosmology: theory – Methods: Numerical – Galaxies: Intergalactic Medium – Galaxies: formation

1 INTRODUCTION

Energy feedback from star formation (SF) and powerful supernovae (SNe) explosions are believed to eject gas from galaxies driving outflows called *galactic*

*winds*¹ (e.g., Johnson & Axford 1971; Mathews & Baker 1971; Larson 1974; Veilleux, Cecil & Bland-Hawthorn

¹ Here, we use the terms *wind* and *outflow* synonymously, meaning continuous outward flow of gas from a galaxy, which might or might not escape depending on its velocity and galactic potential.

* E-mail: pbarai@oats.inaf.it

2005). SNe-driven outflows are detected in many observations at low redshifts (e.g., Lynds & Sandage 1963; McCarthy, van Breugel & Heckman 1987; Bland & Tully 1988; Heckman, Armus & Miley 1990; Lehnert & Heckman 1996; Strickland et al. 2000, 2004; Rupke, Veilleux & Sanders 2005), reaching velocity as high as 1000 km/s (Diamond-Stanic et al. 2012), and at high- z (e.g., Franx et al. 1997; Pettini et al. 2001; Adelberger et al. 2003; Shapley et al. 2003; Erb et al. 2012; Newman et al. 2012b), extending up to distances of 60 – 130 kpc physical (e.g., Lundgren et al. 2012).

We use the term circumgalactic medium (CGM) to denote the gas-phase structures, excluding star-forming gas, within the virial radius of galaxies. Galactic winds are considered to be the primary mechanism by which metals are ejected out of star-forming regions in galaxies and deposited into the CGM and the intergalactic medium (IGM) (e.g., Larson & Dinerstein 1975; Aguirre et al. 2001; Scannapieco, Ferrara & Madau 2002; Aracil et al. 2004; Fox et al. 2007; Bouche et al. 2007; Kawata & Rauch 2007; Pieri, Martel & Grenon 2007; Pinsonneault, Martel & Pieri 2010; Gauthier & Chen 2012; Hummels et al. 2012). The IGM can also be metal-enriched by active galactic nuclei (AGN) feedback (e.g., Khalatyan et al. 2008; Germain, Barai & Martel 2009) and heated by blazars (e.g., Puchwein et al. 2012).

SNe and starburst driven outflow is an important source of feedback in galaxy evolution, and constitute a key ingredient of current galaxy formation studies, both in hydrodynamic simulations (e.g., Springel & Hernquist 2003, hereafter SH03, Schaye et al. 2010) and in semi-analytical models (e.g., Benson et al. 2003; Bertone, Stoehr & White 2005). The winds act by removing gas available to make stars, hence quench SF, and are argued to suppress the formation of low-mass galaxies, flattening the low mass end of the luminosity function in simulations (e.g., Theuns et al. 2002; Rasera & Teyssier 2006; Stinson et al. 2007), which is closer to observations. Feedback is invoked to reproduce the realistic disk galaxies (e.g., Weil, Eke & Efstathiou 1998; Sommer-Larsen, Gotz & Portinari 2003; Governato et al. 2004; Robertson et al. 2004; Okamoto et al. 2005). These outflows are also argued to affect the large column density parts of the Lyman- α absorption line forest (LLSs, subDLAs and DLAs) seen in the spectra of distant quasars, which traces the IGM matter distribution (e.g., McDonald et al. 2005; Kollmeier et al. 2006; Tescari et al. 2011; Viel, Schaye & Booth 2012).

The detailed internal physics underlying the origin and driving of galactic outflows is complex, occurring on scales proper of the multiphase structure of the interstellar medium (ISM) (e.g., Heckman 2003; Stringer et al. 2012). The gas is likely accelerated either by thermal pressure (e.g., Chevalier & Clegg 1985), radiation pressure (e.g., Murray, Quataert & Thompson 2005; Sharma, Nath & Shchekinov 2011; Chattopadhyay et al. 2012; Zhang & Thompson 2012), ram pressure, cosmic rays (e.g., Samui, Subramanian & Srianand 2010; Uhlig et al. 2012); or a combination of them (e.g., Nath & Silk 2009; Everett, Schiller & Zweibel 2010; Sharma & Nath 2012). Cosmological simulations do not resolve the scales at which these physical processes actually happen. Outflows are hence implemented in a phenomenological way in the simulations

using sub-resolution prescriptions and their interplay with the larger-scale environments is investigated.

Energy ejection by SNe and starburst in galaxies, often in the form of powerful outflows, can be incorporated in a number of ways as a source of feedback in the numerical scheme of cosmological simulations. A thermal feedback, where SNe energy is distributed as heating energy of neighboring gas, is well-known to be ineffective (e.g., Katz 1992; Friedli & Benz 1995; Steinmetz & Muller 1995; Katz, Weinberg & Hernquist 1996), because the dense star-forming gas has high cooling rate, and the injected thermal energy is radiated away quickly before it can significantly impact the gas. Therefore depositing the SNe energy in the kinetic form is a more popular implementation in the literature, which has been shown to have significant feedback effects (e.g., Navarro & White 1993; Mihos & Hernquist 1994; Cen & Ostriker 2000; Kawata 2001; Springel & Hernquist 2003; Dalla Vecchia & Schaye 2008; Dubois & Teyssier 2008; Oppenheimer et al. 2012). In our current work we adopt this kinetic feedback by giving a velocity kick to the affected gas.

Alternative forms of SNe feedback have also been implemented for example by considering that the affected gas undergoes adiabatic evolution (e.g., Mori et al. 1997; Thacker & Couchman 2000; Brook et al. 2005); by turning off radiative cooling temporarily for part of the neighboring gas (e.g., Governato et al. 2007; Piontek & Steinmetz 2011); or by distributing SNe energy to hot and cold gas phases separately (e.g., Marri & White 2003; Scannapieco et al. 2006; Murante et al. 2010). Note that few studies have proposed prescriptions for efficient thermal feedback in SPH simulations (e.g., Kay, Thomas & Theuns 2003; Dalla Vecchia & Schaye 2012).

Our kinetic feedback models (§2.2, §2.3) are based on the so-called *energy-driven wind* scenario originally proposed by SH03, and subsequently used by others (e.g., Tornatore et al. 2004; Nagamine et al. 2007; Dalla Vecchia & Schaye 2008; Tescari et al. 2009; Fabjan et al. 2010; Barnes et al. 2011). Here, a fraction of SNe energy provides the outflow kinetic energy, and the wind speed is independent of galaxy mass or SF rate. If we consider the underlying physics, which occurs on scales orders of magnitude below the scales resolved in cosmological simulations, such an outflow is likely to be driven by the thermal pressure of SNe, and might be (more physically) called a *thermally-driven wind*.

Other wind models in cosmological simulations generally involve a different formulation of outflow velocity and wind mass loading factor (described more in §2.2) in terms of galaxy properties (mass, velocity dispersion, SFR), sometimes suggested by observations. Oppenheimer & Davé (2006) implemented *momentum-driven wind*, (also e.g., Tescari et al. 2009, 2011), using analytical prescriptions from Murray, Quataert & Thompson (2005) for momentum injection provided by radiation pressure of photons and SNe (or, *radiatively-driven wind*). Okamoto et al. (2010) investigated models in which the outflow properties are dependent on the local velocity dispersion of the dark matter. Choi & Nagamine (2011) developed a multicomponent and variable velocity galactic outflow model. Puchwein & Springel (2012) implemented a halo mass dependent energy-driven outflow model. Schaye et al. (2010)

compared a number of models of both energy-driven and momentum-driven outflows: few constant-mass loading and constant-velocity cases; mass loading and velocity dependent on gas density, gravitational potential, and halo circular velocity; wind particles temporarily decoupled hydrodynamically versus not decoupled; and thermal injection of SNe energy.

In this paper we explore new wind models, where the galactic outflow speed is a function of radius (distance from galaxy center), as motivated by recent observations (Steidel et al. 2010). We investigate both the cases of a mass-independent dependence on radius, and a halo mass dependent parametrization of the radially varying wind. To our knowledge, this is the first numerical implementation of both of these outflow models.

This paper is organised as follows: we describe our numerical code and simulation setup in §2, in §3 we present and discuss our results, while in §4 we give a summary of the main findings and discuss possible future applications.

2 NUMERICAL METHOD

We use a modified version of the TreePM (particle mesh) - SPH (smoothed particle hydrodynamics) code GADGET-3, whose first version was described in Springel, Yoshida & White (2001). The public release of the code (GADGET-2, Springel 2005) contains a time integration using energy and entropy conserving formulation of SPH (Springel & Hernquist 2002), uses fully adaptive smoothing lengths, and a standard SPH artificial viscosity prescription (Monaghan 1997). GADGET-3 includes a more efficient domain decomposition to improve the workload balance over GADGET-2.

Some of the additional subgrid physics² included in the semi-public version of GADGET-3 code we use are outlined in §2.1. The general galactic wind feedback model is described in §2.2, our new outflow models in §2.3, and the code implementations in §2.4. The simulations we perform are presented in §2.5.

2.1 Sub-resolution Physics: Radiative Processes, SF, Chemical Evolution

Radiative cooling and heating is based on the original implementation of Katz, Weinberg & Hernquist (1996) and improved by adding metal-line cooling which is implemented by adopting the cooling rates from the tables of Wiersma, Schaye & Smith (2009). Net cooling rates are computed element-by-element tracking 11 species: H, He, C, Ca, O, N, Ne, Mg, S, Si, Fe. A spatially-uniform time-dependent photoionizing background radiation is considered from the cosmic microwave background (CMB) and the Haardt & Madau (2001) model for the ultraviolet/X-ray background produced by quasars and galaxies. Contributions from the 11 elements are interpolated as a function of density, temperature and redshift from tables that have

² By *subgrid* we mean *sub-resolution*, referring to physical processes occurring at length scales smaller than the resolved scales in our simulations.

been pre-computed using the public photoionization code CLOUDY (last described by Ferland et al. 1998), assuming the gas to be dust free, optically thin and in (photo)ionization equilibrium.

SF and SNe feedback are implemented following the effective subresolution model by SH03. In this model, the physics of multiphase structure of the ISM, on scales unresolved in cosmological simulations, is modeled using spatially averaged properties describing the medium on scales that are resolved. Gas particles with density above a limiting threshold, $n_{\text{SF}} = 0.13 \text{ cm}^{-3}$ (in units of number density of hydrogen atoms), are considered to contain two phases: cold condensed clouds that are in pressure equilibrium with ambient hot gas. Each gas particle represents a region of the ISM, where the cold clouds supply the material available for SF. Star particles are collisionless, and are spawned from gas particles undergoing SF, according to the stochastic scheme introduced by Katz, Weinberg & Hernquist (1996). We allow a gas particle to spawn up to four generations of star particles; therefore a typical star particle mass is about one-fourth of the initial mass of gas particles.

Stellar evolution and chemical enrichment feedback are implemented following the chemical evolution model of Tornatore et al. (2007). Production of 9 different metal species (C, Ca, O, N, Ne, Mg, S, Si, Fe) are accounted for using detailed yields from Type Ia SN (SN-Ia), Type II SN (SN-II), along with low and intermediate mass stars (LIMS) in the thermally pulsating asymptotic giant branch (TP-AGB) phase. Contributions from both SN-Ia and SN-II to thermal feedback are considered. Mass-dependent time delays with which different stellar populations release metals are included, adopting the lifetime function by Padovani & Matteucci (1993). Different stellar yields are used: for SN-Ia taken from Thielemann et al. (2003), SN-II from Woosley & Weaver (1995), and LIMS from van den Hoek & Groenewegen (1997). The mass range for SN-II is considered to be $M/M_{\odot} > 8$, while that for SN-Ia originating from binary systems is $0.8 < M/M_{\odot} < 8$ with a binary fraction of 10%.

We include a fixed stellar initial mass function (IMF) according to the formalism given by Chabrier (2003), which is a power-law at $M/M_{\odot} > 1$ and has a log-normal form at masses below. However, we use power-law IMFs with different slopes over the whole mass range of 0.1 to $100M_{\odot}$, which mimics the log-normal form of Chabrier (2003) at lower masses, as tests indicate. In our model the functional form: $\phi(M) = KM^{-y}$, is composed of 3 slopes and normalizations: $y = 0.2$ and $K = 0.497$ for stellar masses $0.1 \leq M/M_{\odot} < 0.3$, $y = 0.8$ and $K = 0.241$ for $0.3 \leq M/M_{\odot} < 1$, and $y = 1.3$ and $K = 0.241$ for $1 \leq M/M_{\odot} < 100$. Stars within a mass interval $[8 - 40]M_{\odot}$ become SNe first before turning into black holes (BHs) at the end of their lives, while stars of mass $> 40M_{\odot}$ are allowed to directly end in BHs.

The chemical evolution model also incorporates mass loss through stellar winds and SNe explosions, which are self-consistently computed for a given IMF and lifetime function. A fraction of a star particle's mass is restored as diffuse gas during its evolution, and distributed to the surrounding gas particles. There is no AGN feedback in our simulations.

2.2 Galactic Wind Feedback

We use subgrid models for kinetic feedback via SNe-driven galactic outflows, following the *energy-driven* prescription (§1) (originally from SH03), where the mass and energy carried away by outflows are regulated by two equations. The first equation relates the wind mass-loss rate \dot{M}_w to the SF rate \dot{M}_\star :

$$\dot{M}_w = \eta \dot{M}_\star. \quad (1)$$

Here η is the wind mass loading factor, or the wind efficiency. Observations have shown that in galaxies outflow mass-loss rates are comparable to or few times larger than SF rates (e.g., Martin 1999; Pettini et al. 2002; Bouche et al. 2012; Newman et al. 2012a). Thus, following SH03, we adopt a constant $\eta = 2$ as the efficiency factor.

The other equation relates the wind kinetic energy to a fixed fraction χ of SNe energy:

$$\frac{1}{2} \dot{M}_w v_w^2 = \chi \epsilon_{SN} \dot{M}_\star. \quad (2)$$

Here v_w is the wind velocity, ϵ_{SN} is the average energy released by SNe for each M_\odot of stars formed under the instantaneous recycling approximation. Combining Eqs. (1) and (2), v_w can be re-written as:

$$v_w = \left(\frac{2\chi\epsilon_{SN}}{\eta} \right)^{1/2}. \quad (3)$$

Unlike SH03, and following Tornatore et al. (2007) and Tesfari et al. (2011), we choose v_w as a free parameter in our models, from which the effective χ can be computed using Eq. (3).

For our adopted Chabrier power-law IMF (§2.1), $\epsilon_{SN} = 1.1 \times 10^{49}$ erg M_\odot^{-1} . We initialize the wind energy fraction using $v_w = 400$ km/s, which is the constant velocity of our simulation run CW (§2.5). It corresponds to $\chi = 0.29$ of SNe energy being carried away by the wind.

Outflow models implemented in the GADGET code generally involve different scaling relations of v_w and η in terms of galaxy velocity dispersion, mass, and/or SFR. For the original energy-driven outflows, v_w and η are constant. The momentum-driven wind prescription by Oppenheimer & Davé (2006, 2008) has $v_w \propto \sigma \sqrt{(L/L_{\text{crit}}) - 1}$ and $\eta \propto 1/\sigma$, where σ is the galaxy velocity dispersion, and L/L_{crit} is its luminosity in units of a critical value. In Choi & Nagamine (2011)'s model, $v_w \propto \text{SFR}^{1/3}$ and η is a function of galaxy stellar mass. Puchwein & Springel (2012) assumed v_w and η to be proportional to halo mass.

However, any dependence of v_w on galactocentric radius (or distance from galaxy center) has not been explored before and this is what we are going to do in the present work.

2.3 Wind Velocity Dependent on Galactocentric Distance, $v_w(r)$

The new subgrid wind model is motivated by the recent observational studies of Steidel et al. (2010). Studying the metal-enriched gas kinematics in a region of ~ 125 kpc around star-forming (Lyman-break) galaxies at redshifts $z = 2 - 3$, they are able to reproduce their spectroscopic

data using a simple model for outflows and circumgalactic gas. Considering a spherically-symmetric gas flow, quantities are parameterized as a function of galactocentric distance, or radius r . The outflow acceleration is described as a power-law function of r :

$$a(r) \propto r^{-\alpha} = \frac{dv(r)}{dt} = \left[\frac{dv(r)}{dr} \right] \left(\frac{dr}{dt} \right) = v(r) \left[\frac{dv(r)}{dr} \right]. \quad (4)$$

Such a power-law acceleration have also been adopted recently by Gauthier & Chen (2012). Integrating this equation with appropriate boundary conditions one can get the outward velocity $v(r)$, which is given in Eq. (16) of Steidel et al. (2010). We adopt a similar expression for the radially-varying velocity of galactic winds, namely:

$$v_w(r) = v_{\text{max}} \left(\frac{r_{\text{min}}^{1-\alpha} - r^{1-\alpha}}{r_{\text{min}}^{1-\alpha} - R_{\text{eff}}^{1-\alpha}} \right)^{0.5}. \quad (5)$$

Here r_{min} is the distance from which the wind is launched and where the velocity is zero, R_{eff} represents the outer edge of gas distribution, v_{max} is the velocity at R_{eff} and α is a power-law index. In Table 5 of Steidel et al. (2010), the authors fit spectral line observations (of Ly α , CIV, CII, SIII, SiIV) using different parameter values ranging between: $70 \leq R_{\text{eff}} \leq 250$ kpc, and $650 \leq v_{\text{max}} \leq 820$ km/s. Assuming $r_{\text{min}} = 1$ kpc, they find that combinations of α within the range $1.15 \leq \alpha \leq 1.95$ together with another covariant parameter, can adequately reproduce observed ISM line profiles. In the absence of a unique set of parameter values, we choose the following for one of our simulations (run RVWa, §2.5): $r_{\text{min}} = 1 h^{-1}$ kpc, $R_{\text{eff}} = 100 h^{-1}$ kpc, $v_{\text{max}} = 800$ km/s, and $\alpha = 1.15$.

Such a trend of $v_w(r)$ correlating positively with r has also been found in other observations: for example Veilleux et al. (1994) parameterized outflow velocity as $v_w \propto r^n$ with $2 < n < 3$ for the spiral galaxy NGC3079.

We note that a scenario in which the wind velocity is not unique but has instead any value (fast and/or slow outflow) could possibly result in faster ejecta at large distances from the galaxy center and slower ones closer to the center, since the former would have had more time to travel out to large distances. The model presented here could mimic such a behaviour.

We explore a further halo mass dependent parametrization of our new wind model in run RVWb (§2.5). Observational studies of ultraluminous infrared galaxies at $z = 0.042 - 0.16$ by Martin (2005) detect a positive correlation of galactic outflow speed with galaxy mass. Their Figure 7 (bottom panel) shows that the outflow terminal velocities are always 2 – 3 times larger than the galactic rotation speed. Inspired by these results, we assume that the velocity v_{max} is related to the circular velocity v_{circ} of the halo at the virial radius R_{200} as:

$$v_{\text{max}} = 2v_{\text{circ}} = 2\sqrt{\frac{GM_{\text{halo}}}{R_{200}}}. \quad (6)$$

The halo mass M_{halo} and radius are related such that R_{200} encloses a density 200 times the mean density of the Universe at the simulation redshift z :

$$M_{\text{halo}} = \frac{4\pi}{3} R_{200}^3 (200\rho_{\text{crit}}\Omega_{M,0}) (1+z)^3. \quad (7)$$

Here $\rho_{\text{crit}} = 3H_0^2/(8\pi G)$ is the present critical density. The assumption during code implementation is that the total group mass obtained by our group finder (§2.4) is the virial halo mass and that it is collapsing at the simulation redshift. Using such a prescription the resulting dependence of maximum velocity on halo mass and redshift is:

$$v_{\text{max}} \propto M_{\text{halo}}^{1/3} (1+z)^{1/2}. \quad (8)$$

We also set the effective radius as:

$$R_{\text{eff}} = R_{200} \propto M_{\text{halo}}^{1/3} (1+z)^{-1}, \quad (9)$$

because v_{max} is the model wind velocity at R_{eff} .

2.4 Implementation in the GADGET-3 code

Our new wind model described in §2.3 requires an extra parameter: the distance of gas particles from their host galaxy center. We identify galaxies by running a Friends-of-Friends (FOF) group finder on-the-fly within our GADGET-3 simulations. Given a *linking length*, L_{gr} , the FOF algorithm finds a group by selecting all particles that lie within a distance L_{gr} from any other particle in the group.

Firstly, an average inter-particle distance, L_p , is calculated; using the total mass, number of particles and the mean density. The linking length for the default on-the-fly FOF in GADGET-3 is $L_{gr}/L_p = 0.16$, which is commonly used to find dark matter (DM) halos. However, sometimes the FOF can link together DM substructures which actually belong to multiple galaxies with distinct stellar structures, into a single halo. Therefore, the stellar components of the FOF groups are considered to be more stable and thereby identified as galaxies.

In order to select galaxies, we obtain stellar groups by modifying the FOF group finder as follows: we allow the FOF to first link over stars as the primary particle type, and then link over (gas + DM) particles as the secondary type. To facilitate selection of stellar groups, which are generally smaller in size, we use a linking length three times smaller than the default one: $L_{gr}/L_p = 0.16/3$. The FOF is executed on-the-fly within a simulation at time intervals of a multiplicative factor 1.001 of the scale factor a , or, $a_{\text{next}}/a_{\text{prev}} = 1.001$. All the groups above a minimum length of ≥ 32 particles are finally selected, which provide us with a set of galaxies at a given simulation time. The code execution comprises of a FOF overhead of (6–9)% of the total processing time.

Our preliminary tests indicate that the center-of-mass position of the FOF groups are offset from the gas density peak location. Hence we decide not to consider the center-of-mass positions but to record the position of the member gas particle with maximum SPH density in each group: this maximum gas density location is considered as the group center. We tag in the code the group (representing a galaxy) and the group center each relevant gas particle belongs to. We define the galactocentric radius, r , as the distance of each gas particle from its group center.

Assuming that outflows are generated from mass loss during SF, the implementation of launching the wind involves a probabilistic criteria similar to spawning star particles, as described in SH03. Gas particles undergoing SF are stochastically selected and kicked into wind, by impart-

ing an one-time v_w boost. A probability is calculated in a timestep Δt for each multiphase gas particle:

$$p = 1 - \exp\left(-\frac{\eta x \Delta t}{t_{\text{sfr}}}\right). \quad (10)$$

Here x is the mass fraction of cold clouds and t_{sfr} is the SF timescale, which depends on the parameters of the SF model. A random number is drawn in the interval $[0, 1]$, and if it falls below p then the particle is given a wind kick. If \vec{v} is particle velocity and ϕ its gravitational potential, then its velocity after receiving wind kick is updated to:

$$\vec{v}_{\text{new}} = \vec{v}_{\text{old}} + v_w \hat{y}. \quad (11)$$

The direction of the unit vector \hat{y} is set along $(\vec{v}_{\text{old}} \times \vec{\nabla}\phi)$ or $-(\vec{v}_{\text{old}} \times \vec{\nabla}\phi)$, randomly selected between the two. This makes the wind particles to be preferentially ejected along the rotation axis of the galaxy or perpendicular to the galaxy disk.

In order to enable the outflow to escape from dense SF regions without affecting the SF, a new wind particle (gas particle just receiving a wind kick following Eq. 11) is decoupled from hydrodynamic interactions, for a maximum duration $t_{\text{dec}} = 0.025t_{\text{H}}(z)$, where $t_{\text{H}}(z)$ is the Hubble time at a relevant simulation redshift. Then the wind particle does not enter hydrodynamic force computation in the code, but is included in gravity and SPH density calculation. If the particle's density has fallen below $n_{\text{dec}} = 0.25n_{\text{SF}}$, then the decoupling is stopped before t_{dec} , and full hydrodynamics are enabled again. In our simulations, the majority of wind particles end their decoupling phase following the density condition.

Summarizing, the main free parameters in the wind model are v_w and η , along with t_{dec} and ρ_{dec} for the decoupling prescription. The wind velocity is either constant (Eq. 3, §2.2), or dependent on radius (Eq. 5) and halo mass (Eq. 8).

In this Section we have shown the actual implementation of different forms of v_w , including radial and mass dependence of velocity which are observationally motivated. We later study the implications such models have on the CGM and IGM properties in the simulated volume.

2.5 Simulations

The series of simulations we perform are listed in Table 1. A cosmological volume, with periodic boundary conditions, is evolved starting with an equal number of DM and gas particles from $z = 99$, where the initial conditions have been generated using the CAMB³ software (Lewis et al. 2000), up to $z = 2$. A concordance flat Λ CDM model is used with the following parameters: $\Omega_{M,0} = 0.2711$, $\Omega_{\Lambda,0} = 0.7289$, $\Omega_{B,0} = 0.0463$, $n_s = 0.96$, $\sigma_8 = 0.809$, $H_0 = 70.3 \text{ km s}^{-1} \text{ Mpc}^{-1}$, in agreement with recent observations of the cosmic microwave background radiation, weak gravitational lensing, Lyman- α forest and mass function evolution of galaxy clusters (e.g., Lesgourgues et al. 2007; Vikhlinin et al. 2009; Komatsu et al. 2011).

The smaller box-size $L_{\text{box}} = 5h^{-1} \text{ Mpc}$ comoving series (or, box *SB*) has $N_{\text{part}} = 2 \times 128^3$ DM and gas particles

³ <http://camb.info/>

Table 1. Simulation Parameters. Column 1: Name of simulation run. Names ending with "t" are smaller boxsize runs SB, and LB are runs with larger boxsize, all of which are stopped at $z \sim 2$. Column 2: $L_{\text{box}} =$ Comoving side of cubic simulation volume. Column 3: Specifications of galactic wind feedback model. Parameters of SB runs: Number of gas and DM particles in the initial condition, $N_{\text{part}} = 2 \times 128^3$. Mass of gas particle (which has not undergone any star-formation), $m_{\text{gas}} = 7.66 \times 10^5 h^{-1} M_{\odot}$. Gravitational softening length (of all particle types), $L_{\text{soft}} = 0.98 h^{-1}$ kpc. In runs RVWat and RVWa, parameters of radially varying wind model (§2.3): $r_{\text{min}} = 1 h^{-1}$ kpc, $R_{\text{eff}} = 100 h^{-1}$ kpc, $v_{\text{max}} = 800$ km/s, $\alpha = 1.15$. In runs RVWbt and RVWb, parameters of radially varying wind model dependent on halo mass (§2.3): $v_{\text{max}} = 2 \sqrt{GM_{\text{halo}}/R_{200}}$, and $R_{\text{eff}} = R_{200}$. Parameters of LB runs: $N_{\text{part}} = 2 \times 320^3$, $m_{\text{gas}} = 6.13 \times 10^6 h^{-1} M_{\odot}$, $L_{\text{soft}} = 1.95 h^{-1}$ kpc.

Run Name	L_{box} [h^{-1} Mpc]	Galactic Wind Feedback
Smaller-Box Runs : SB		
NWt	5	No Wind
CWt	5	Energy-driven constant-velocity $v = 400$ km/s
RVWat	5	Radially varying with fixed parameters
RVWbt	5	RVW with halo mass dependent parameters
Larger-Box Runs : LB		
NW	25	No Wind
CW	25	Energy-driven constant-velocity $v = 400$ km/s
RVWa	25	Radially varying with fixed parameters
RVWb	25	RVW with halo mass dependent parameters

in the initial condition. This is the higher resolution series with gas particle mass $m_{\text{gas}} = 7.66 \times 10^5 h^{-1} M_{\odot}$, and DM particle mass $m_{DM} = 4.49 \times 10^6 h^{-1} M_{\odot}$. The Plummer-equivalent softening length for gravitational forces is set to $L_{\text{soft}} = 0.98 h^{-1}$ kpc comoving. In the larger box-size $L_{\text{box}} = 25 h^{-1}$ Mpc comoving series (or, box *LB*) the numbers are: $N_{\text{part}} = 320^3$, $m_{\text{gas}} = 6.13 \times 10^6 h^{-1} M_{\odot}$, $m_{DM} = 3.59 \times 10^7 h^{-1} M_{\odot}$, $L_{\text{soft}} = 1.95 h^{-1}$ kpc. The minimum gas smoothing length is set to a fraction 0.001 of L_{soft} in all the simulations. However the minimum smoothing which is actually achieved in the simulations depend on the resolution, and in our runs the gas smoothing lengths went down to $\sim 0.2 L_{\text{soft}}$. The second set of simulations, at slightly worse resolution compared to the first set, has been chosen in order to increase the statistics, since more number of halos and more massive halos are expected to form in the larger box.

In each series four runs are performed incorporating the same non-wind subgrid physics described in §2.2, and investigating different galactic wind models:

- (1) NW: no wind;
- (2) CW: energy-driven wind with constant velocity (§2.2, Eq. 3) $v_w = 400$ km/s;
- (3) RVWa: radially varying wind with fixed parameters (§2.3) $r_{\text{min}} = 1 h^{-1}$ kpc, $R_{\text{eff}} = 100 h^{-1}$ kpc, $v_{\text{max}} = 800$ km/s, $\alpha = 1.15$; and
- (4) RVWb: radially varying wind with parameters dependent on halo mass.

The smaller box-size runs have an extra *t* appended to the names. Few results are presented for both the box sizes, namely SB and LB runs. While the remaining results are

shown only for one box-size, with the reason given in the relevant parts of §3 next.

The new velocity prescriptions are plotted in Figure 1. The black curve in the left panel shows the outflow velocity as a function of galactocentric radius for the parameters in run RVWa. For comparison, the blue horizontal line denotes the constant value of velocity, $v = 400$ km/s, used in run CW. The right panel depicts the parameterization of v_{max} , or the velocity at R_{eff} in run RVWb, as a function of halo mass for different redshifts of collapse.

We have analyzed the carbon content of the gas in the box, since carbon is one of the most abundant heavy element in the Universe, and the spectral lines produced by ionized carbon are relatively easy to observe. The metallicity of carbon, Z_C , is computed as the ratio of carbon mass to the total particle mass for each gas particle. Abundance ratios are expressed in terms of the Solar metallicity, which is $Z_{C,\odot} = 0.002177$ (mass fraction of carbon in Sun) derived from the compilation by Asplund, Grevesse & Sauval (2005).

3 RESULTS AND DISCUSSION

3.1 Outflow Velocity

The different implementations of the outflow velocity in the SB runs are shown in the panels of Fig. 2: NWt (top-left), CWt (top-right), RVWat (bottom-left), and RVWbt (bottom-right). Here the smaller boxsize is chosen for visualization purposes, to unambiguously distinguish the wind velocity from the remaining gas in the most-massive galaxy within the box volume which has the largest SFR. The

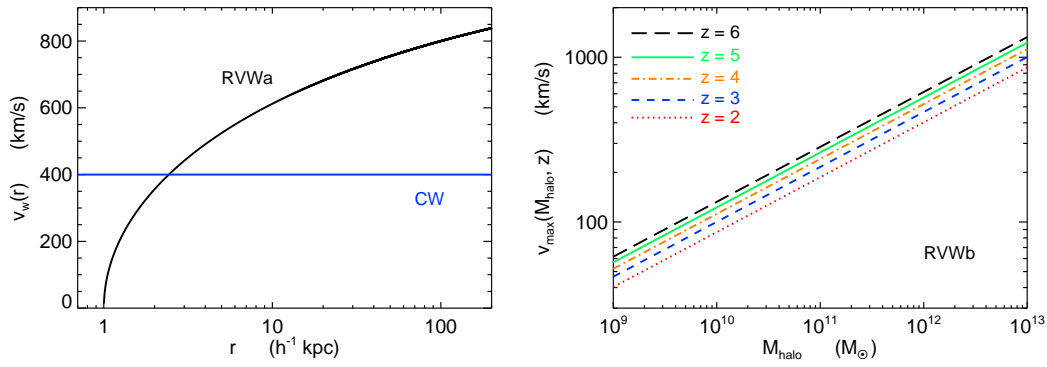


Figure 1. *Left panel:* Black curve is the radial profile of outflow velocity as formulated in Eq. (5), which is implemented in our hydrodynamic simulations motivated by observations of Steidel et al. (2010). The parameter values are for run RVWa (Table 1): $r_{\min} = 1h^{-1}$ kpc, $R_{\text{eff}} = 100h^{-1}$ kpc, $v_{\max} = 800$ km/s, and $\alpha = 1.15$. The blue horizontal straight line denotes the constant value of velocity, $v = 400$ km/s, in run CW. *Right panel:* Velocity at R_{eff} as a function of halo mass, shown in Eqs. (6) and (8), for different redshifts of collapse. Such a formulation is implemented in run RVWb motivated by observational studies of Martin (2005).

trends for the LB runs are the same as the SB results shown here; however for galaxies of this mass range there are fewer wind particles because of lower SFR, since the LB runs produce more massive galaxies with higher SFR in a larger cosmological volume than SB. The velocity magnitude of the gas particles is plotted in Fig. 2 as a function of distance from center of galaxy at $z = 2.44$. As described in §2.4, galaxies are identified on-the-fly in the simulations using a FOF algorithm linking over star particles as the primary type using a linking length 3 times smaller than the default one, and the galaxy center corresponds to the location of the maximum gas density.

All the gas particles lying within a radius of $100h^{-1}$ kpc from group center are shown as black points in Fig. 2. The particles which have recently received a wind kick velocity can be tracked, for the duration of their hydrodynamic decoupling, through their positive decoupling time (§2.4). We call these the *wind-phase particles* and we mark them with the red plus symbols. The median wind-phase particle’s velocity in radial bins is plotted as the green asterisks joined by the green dashed curve. The input subgrid wind velocity (v_w) implemented in the code is instead represented by the blue solid curve. In order to mark the differences clearly, in each run results are stacked over the 20 most-massive galaxies having total halo (DM + gas + stars) mass between $M_{\text{halo}} = (0.9 - 15) \times 10^{10} M_{\odot}$, the exact range for each case is written in the respective panel. The escape velocity, $v_{\text{esc}} = \sqrt{2GM_{\text{halo}}/r}$, for a representative halo mass $M_{\text{halo}} = 10^{11} M_{\odot}$, is shown by the cyan dashed curve. At a given radius, particles moving faster than v_{esc} are unbound to the halo.

Run NWt gives the radial structure of gas velocity without any wind, reaching a maximum of $v \sim 400 - 500$ km/s around galaxies. The other 3 runs have winds implemented and present a distribution of red points. Wind particles are kicked over a radial range from the center up to $r \sim (30 - 50)h^{-1}$ kpc, marking the size of star-forming galaxy disk. These particles gain an additional velocity of v_w during their wind kick (§2.4). Runs CWt and RVWt demonstrate this as some red points clustered around or somewhat above the blue curve. Afterward they move away

from galaxy center and get decelerated, causing a fraction of the red points to fall well below v_w . Therefore, when considering the wind particles at given r , the median velocity (green dashed curve) is somewhat lower than v_w (blue). Run CWt has particles kicked by $v_w = 400$ km/s at all r , while in our new implementation RVWt at the upper envelope of the red points follow the $v_w(r)$ radial profile of Eq. 5. In run RVWbt (bottom-right panel), the blue solid curve shows v_w for the halo mass $M_{\text{halo}} = 10^{11} M_{\odot}$. This turns out to be a weak wind, because most of the gas is moving at velocity above the blue curve at $r \leq 10h^{-1}$ kpc. Hence the wind particles do not move outward appreciably, and end up following a distribution very close to the remaining gas (black points).

Fig. 2 also demonstrates that even though wind particles are kicked only one time according to the original prescription of SH03, since this procedure is done at every timestep (stochastically selecting from all the star-forming particles), the desired v_w is reproduced by multiple gas particles at any given time. The wind particles slow down, but in the next timesteps more particles are kicked out with v_w , as long as there is SF, thus roughly mimicking a continuous outflow of gas moving with given subgrid input speed around a galaxy.

Velocity magnitude histograms of gas particles at $z = 2.91$ are plotted in Fig. 3, showing mass fraction in velocity bins; wind (gas) particles are represented by solid (dashed) curves. In each case the histogram is normalized to the total gas mass in the respective simulation. The SB runs are shown in the left panel where the maximum particle velocity is ~ 700 km/s, and LB runs in the right panel where particles reach ~ 1100 km/s because of higher-mass halos forming in a larger box.

Runs CWt and CW have peaks in their wind particle velocity histogram at $v \sim 400$ km/s, since in this case v_w is kept constant at this value. The wind velocity histogram is much flatter in runs RVWt and RVWa with no well-defined peak, because v_w has a range of values depending on galactocentric distance. Runs RVWbt and RVWb also have a peak wind velocity, which is at a lower value $v \sim 100 - 200$ km/s, corresponding to the outflow of lower-mass halos which are

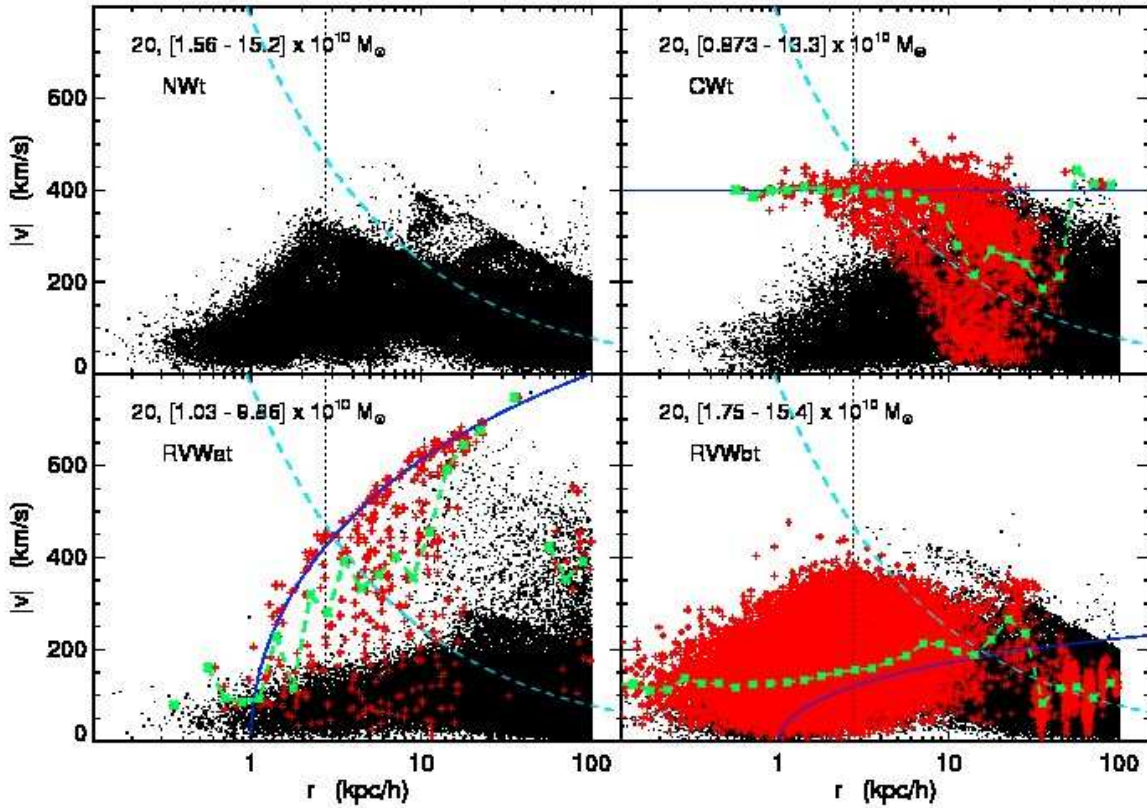


Figure 2. Velocity magnitude of the gas as a function of distance from galaxy center at $z = 2.44$ in the SB runs with different wind models: no wind (top-left), energy-driven constant-velocity wind (top-right), radially varying wind with fixed parameters (bottom-left), and radially varying wind with parameters dependent on halo mass (bottom-right). All the gas particles within $100h^{-1}$ kpc from the group center are shown as black points. In the runs with wind, the red plus symbols are the wind-phase particles (described in §3.1), whose median velocity in radial bins is denoted by the green asterisks joined by the green dashed curve. The blue solid curve represents the subgrid wind velocity implemented in the code in each case; in the last panel (run RVWbt) the blue solid line refers to a representative halo mass $M_{\text{halo}} = 10^{11} M_{\odot}$. Each panel shows the stacked result of the 20 most-massive galaxies having total mass within the range specified in the panels. The vertical black dotted line denotes the resolved length scale of Newtonian gravitational forces ($2.744h^{-1}$ kpc in the SB runs), which is 2.8 times $L_{\text{soft}} = 0.98h^{-1}$ kpc comoving. The cyan dashed curve shows the escape velocity, $v_{\text{esc}} = \sqrt{2GM_{\text{halo}}/r}$, for the representative halo mass.

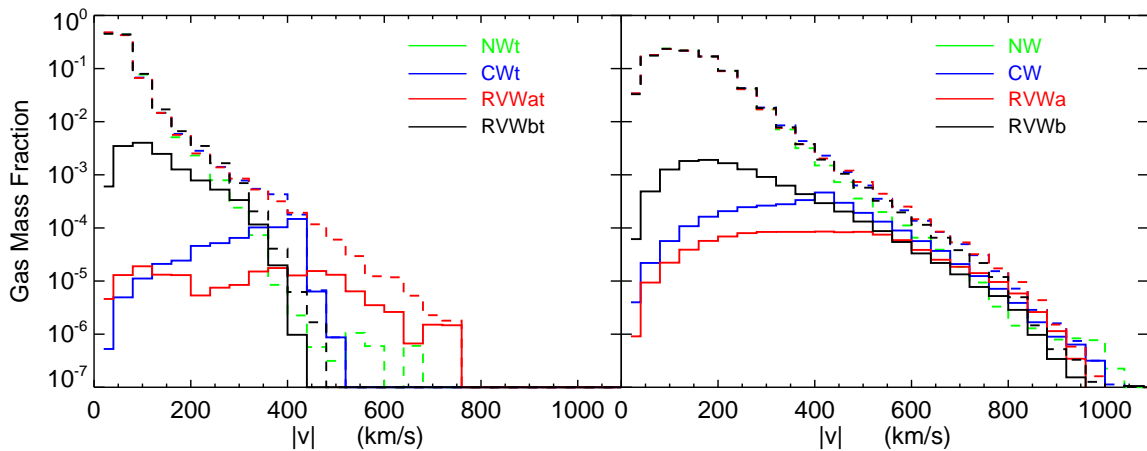


Figure 3. Velocity magnitude histogram of wind particles (solid), and all gas particles (dashed) at $z = 2.91$, showing the mass fraction of gas per velocity bins. The SB runs are in the left panel and LB runs are in the right panel, in each case the histogram is normalized to the total gas mass in the simulation at the redshift considered.

more numerous in hierarchical structure formation. Considering all the gas particles, the no-wind (NW) run has slightly higher mass fraction at $v \leq 300$ km/s (not distinguishable in the plot), while runs with wind (CW, RVWa, RVWb) have higher gas mass with $v \geq 300$ km/s.

3.2 Star Formation Rate

3.2.1 Global Star Formation Rate Density

The global star formation rate density (SFRD) as a function of redshift is plotted in Fig. 4, for the SB runs in the left panel, and for the LB runs in the right one; in each panel the four wind models are labeled by the different colors and plotting symbols. The SFRD is computed by summing over all the SF occurring in the whole simulation box and dividing it by the time-step interval and box volume to obtain the rate density in $M_{\odot} \text{ yr}^{-1} \text{ Mpc}^{-3}$. Galactic wind feedback clearly has significant impact on SFRD, reducing SF several times depending on the outflow model.

Between $z \sim 8 - 10$, there is already a trend of suppression of SFRD with winds as the CW run has 1.2 times lower SFRD than NW, while at $z < 8$ the SFRDs of the runs diverge more. The differences are small between runs RVWb and NW; in RVWb the SFRD values are 1.5 – 2 times smaller than NW between $z \approx 3 - 8$, and agree with NW at $z \approx 2 - 3$, making RVWb the wind model least effective in suppressing SF. There is however a substantial reduction of SFRD in runs CW and RVWa. The SB box have a stronger wind-driven suppression; SFRD is 12 times smaller in RVWat (and 5 times smaller in CWt) than NWt at $z < 3$. While in the LB box, the reduction is 4 times in RVWa and 2 times in CW at $z < 4$. Analyzing the effective wind models, RVWa has 1.2 times higher SFRD than CW from high z up to $z = 5$, but later RVWa suppresses it more and produces 2 – 4 times lower SFRD at $z = 2$.

Effects of box-size and resolution are visible in our results. The $z = 12$ SFRD is ~ 2 higher in the SB box than LB, because the SB series has higher resolution, and can track denser gas, forming more stars. However at $z < 3 - 4$, the RVWat run of SB series produces 2 – 3 times lower SFRD than RVWa of LB, one reason for which is the relevant box-size; the halos forming in box SB are less-massive and fewer in number than in LB. Studying the shape of the SFRD evolution, the SB runs tend to show a peak in SFRD at a certain redshift: $z = 2.5$ in NWt and RVWbt, $z \leq 2$ in CWt, and $z = 4$ in RVWat. Whereas all the LB runs have a plateau of SFRD between $z = 2 - 3.5$.

Observational data are overplotted in Fig. 4 with the cyan symbols and error bars. Each data set is shown with a different plotting symbol as listed next. These data are taken mainly from Cucciati et al. (2012) - *filled circles*, and the compilations therein originally from Steidel et al. (1999) - *asterisks*, Ouchi et al. (2004) - *plus signs*, Perez-Gonzalez et al. (2005) - *inverted triangles*, Schiminovich et al. (2005) - *diamonds*, Bouwens et al. (2009) - *open squares*, Reddy & Steidel (2009) - *crosses*, Rodighiero et al. (2010) - *open circles*, van der Burg, Hildebrandt & Erben (2010) - *upright triangles*, Bouwens et al. (2012) - *filled squares*.

Comparing with observations, we see that no single simulation model can fit the data from a single observation.

Taken collectively, there is a better match of simulations with observations at low- z . At earlier cosmic epochs between $z \sim 4.5 - 10$, SFRD in the simulations is systematically higher, reaching 2 – 10 times the observed values. At later times between $z \sim 2 - 4.5$, most of the observations lie within the ranges of SFRD produced by the different wind models. Run CW of the LB series is the model providing the best-fit to the observations at lower- z .

3.2.2 Specific Star Formation Rate

The specific star formation rate (sSFR) as a function of galaxy stellar mass at $z = 1.98$ is plotted in Fig. 5. The SB runs are in the left panel and the LB runs in the right one; in each panel the four wind models are labeled by the different colors and plotting symbols. The solid curves denote the median value within a mass bin for each run, and the grey shaded area enclose the 70 percentiles above and below the median in runs RVWat and RVWa (red curves) showing the typical scatter. The black dashed line is observational data at $z = 2$ from Daddi et al. (2007), indicating the main sequence (MS) for star forming galaxies, which is parametrized by the form: $\text{SFR} = 200 \left(\frac{M_{\text{stellar}}}{10^{11} M_{\odot}} \right)^{0.9} M_{\odot} \text{ yr}^{-1}$. The black dotted line marks the loci 4 times above the MS. According to Rodighiero et al. (2011), the region between MS and 4-MS encompass a majority fraction of observed galaxies.

Comparing simulation results with observations, we see reasonably good agreement. The median sSFR of all the models in the LB volume (right panel in Fig. 5) lie between the observed MS and 4-MS. In the SB volume (left panel), runs NWt and RVWbt lie within MS and 4-MS, however CWt and RVWat are below MS, for a given stellar mass.

3.3 Galaxy Mass Function and Mass Fraction

The gas and stellar mass function (dN , in units of $(d \log M)^{-1} \text{ Mpc}^{-3}$) of galaxies in the LB runs at $z = 2.23$ is plotted as the solid curves in Fig. 6, left panels. The top-left panel shows the mass function of the gas component in galaxies. All the 4 runs have the same slope between $M_{\text{gas}} \sim (10^9 - 10^{11}) M_{\odot}$, but shifted sideways as described next. NW and RVWb produce almost similar trends: $dN \approx 0.3$ at $(2 - 3) \times 10^9 M_{\odot}$, with the RVWb mass function shifted right-ward by ~ 1.2 mass units (M_{\odot}). Results in CW and RVWa are quite similar, shifted left-ward with respect to NW by $(2 - 3) M_{\odot}$. The wind in these runs expel gas efficiently out of galaxies with $M_{\text{gas}} \geq 10^9 M_{\odot}$, producing a smaller number of objects with such high gas masses. Only at $\geq 10^{10} M_{\odot}$, CW has slightly more galaxies at the same mass than RVWa.

The bottom-left panel of Fig. 6 shows the mass function of the galactic stellar component. Runs CW and RVWa having $dN \approx 0.2 - 0.3$ at $M_{\text{stellar}} = (1.5 - 2) \times 10^8 M_{\odot}$, produce a steeper stellar mass function than NW and RVWb where $dN \approx 0.1$ at $10^9 M_{\odot}$. There is a small excess of galaxies in RVWa compared to CW between $M_{\text{stellar}} = (2 \times 10^8 - 10^9) M_{\odot}$, and a slight excess in NW than RVWb in the range $(10^9 - 10^{10}) M_{\odot}$. The cyan filled circles and error bars represent observational data of the stellar mass function from Marchesini et al. (2009), within $2 \leq z < 3$ (the results

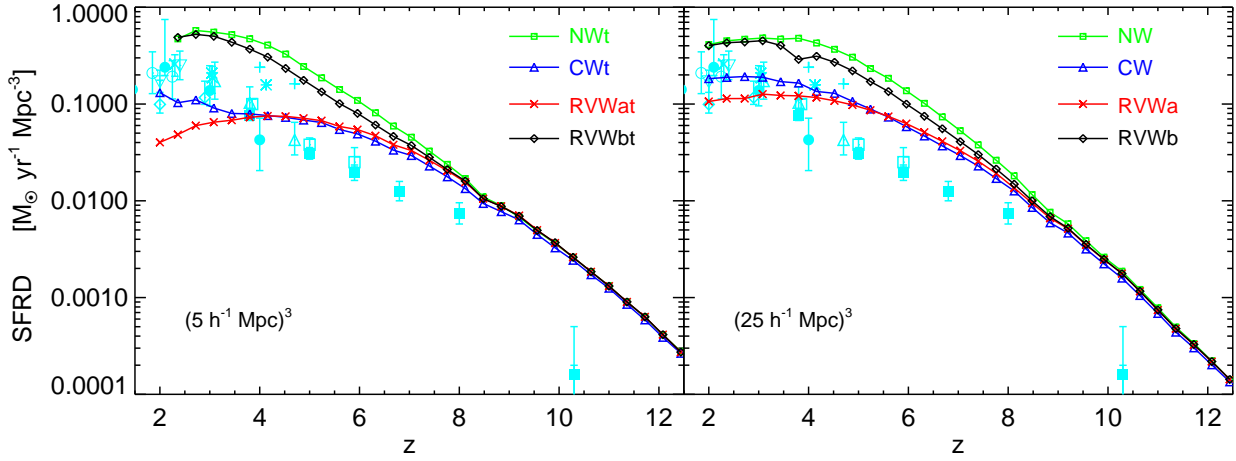


Figure 4. Star formation rate density in whole simulation volume as a function of redshift, for the SB runs in the left and LB in the right panel, with the respective wind models labeled by the color and plotting symbol. The cyan symbols and error bars denote observational data from Cucciati et al. (2012) - *filled circles*, and the compilations therein originally from Steidel et al. (1999) - *asterisks*, Ouchi et al. (2004) - *plus signs*, Perez-Gonzalez et al. (2005) - *inverted triangles*, Schiminovich et al. (2005) - *diamonds*, Bouwens et al. (2009) - *open squares*, Reddy & Steidel (2009) - *crosses*, Rodighiero et al. (2010) - *open circles*, van der Burg, Hildebrandt & Erben (2010) - *upright triangles*, Bouwens et al. (2012) - *filled squares*. Detailed comparison is in §3.2.1.

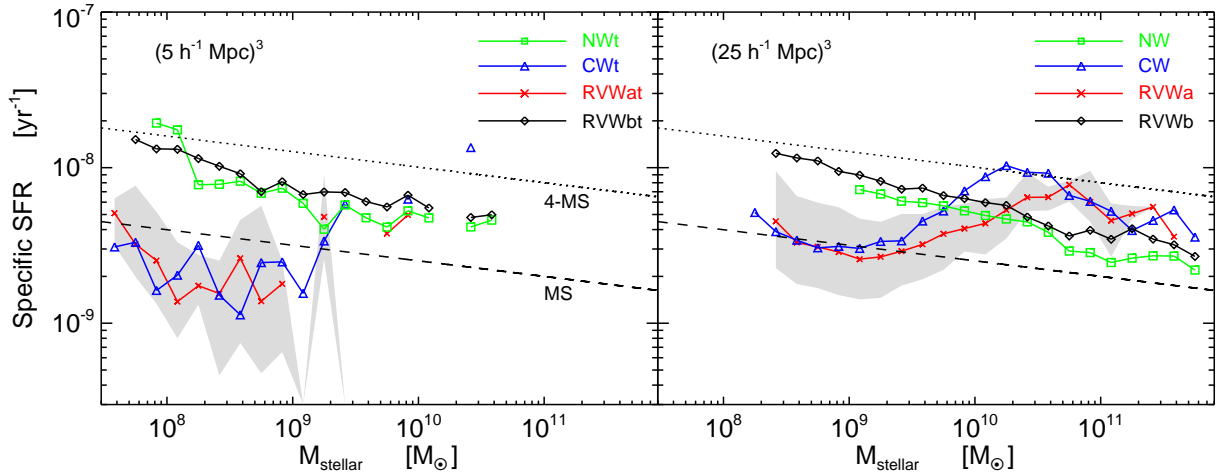


Figure 5. Specific star formation rate as a function of galaxy stellar mass at $z = 1.98$, for the SB runs in the left and LB in the right panel, with the respective wind models labeled by the color and plotting symbol. The solid curves denote the median value within a mass bin for each run, and the grey shaded area enclose the 70 percentiles above and below the median in runs RVWat and RVWa (red curves) showing the typical scatter. The black dashed line is observational data at $z = 2$ from Daddi et al. (2007), indicating the main sequence (MS) for star forming galaxies, $\text{SFR} = 200 \left(\frac{M_{\text{stellar}}}{10^{11} M_{\odot}} \right)^{0.9} M_{\odot} \text{ yr}^{-1}$. The black dotted line marks the loci 4 times above the MS; the region between MS and 4-MS encompass a majority fraction of observed galaxies from Rodighiero et al. (2011).

which are tabulated in their Table 1). Our model RVWa (red curve) provide a reasonably good match to these high- z observations over the mass range $M_{\text{stellar}} = (8 \times 10^9 - 10^{11}) M_{\odot}$. However our stellar mass functions are steeper than that of semi-analytic models by Bower, Benson & Crain (2012) at $z = 0$, and the observational data therein, along with other low- z observations (e.g., Papastergis et al. 2012).

Fig. 6 also shows results of the wind model RVWat from the SB box, plotted as the red dashed curve in each panel. Comparing RVWa and RVWat, the smaller higher-resolution

box has lower-mass halos forming, extending the gas mass function to $M_{\text{gas}} \sim 10^8 M_{\odot}$, and the stellar mass function down to $M_{\text{stellar}} \sim 4 \times 10^7 M_{\odot}$.

The mass fractions of gas and stars in galaxies with respect to total mass of halos are plotted in the right panels of Fig. 6: gas mass fraction in the top-right, and stellar mass fraction in the bottom-right. Solid curves denote the median value within a mass bin for each run labeled by the color and plotting symbol. The grey shaded area encloses the 70th percentiles above and below the median in run RVWa (red

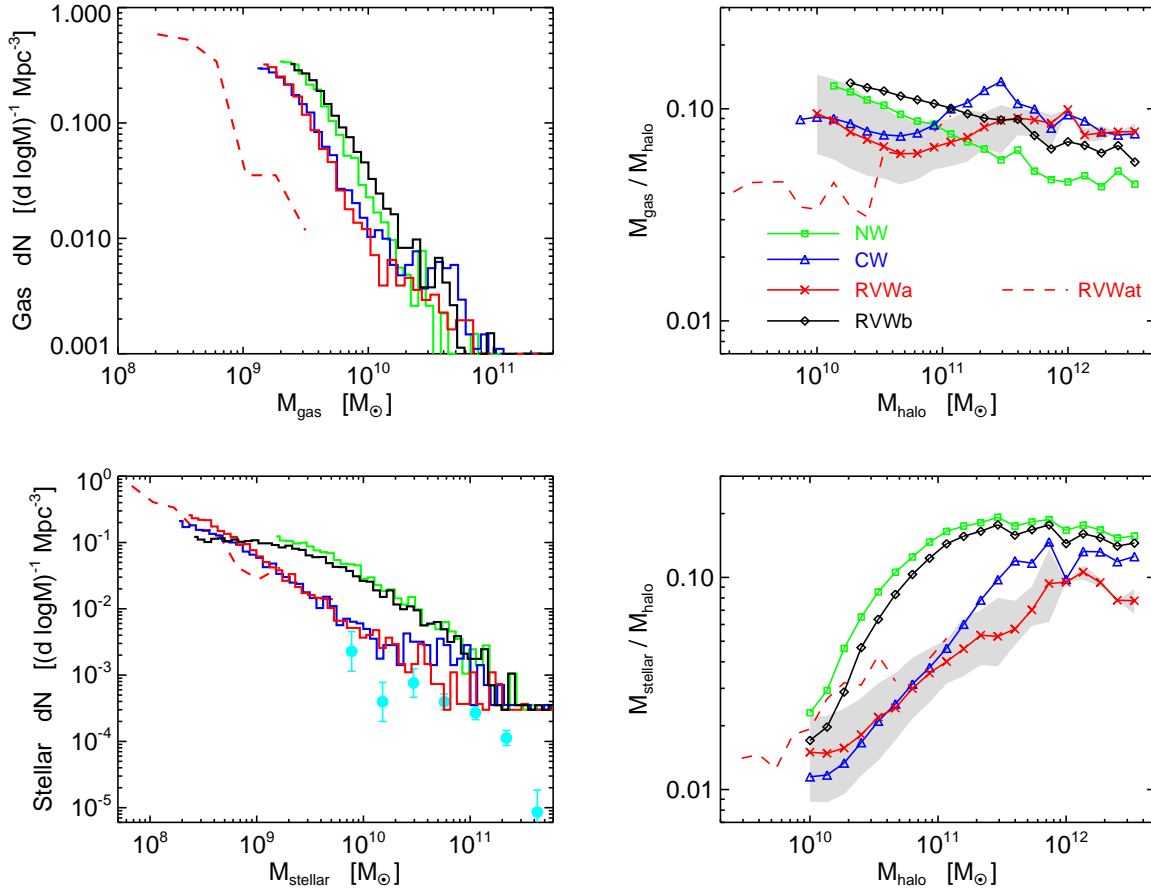


Figure 6. Galaxy gas mass function (top-left), stellar mass function (bottom-left), along with gas mass fraction (top-right) and stellar mass fraction (bottom-right) w.r.t. total mass of halos, at $z = 2.23$, of the LB runs shown as the solid curves. In the right panels the solid curves denote the median value within a mass bin for each run, and the grey shaded area enclose the 70 percentiles above and below the median in run RVWa (red curve) showing the typical scatter. One of the wind model (RVWat) from the SB box is plotted as the red dashed curve in each panel. The cyan filled circles and error bars in the bottom-left panel represent observational data of the stellar mass function from Marchesini et al. (2009), within $2 \leq z < 3$ (the results which are tabulated in their Table 1). Details are given in the text in §3.3.

curve), and show the typical scatter at given halo mass. With no-wind (NW) the gas fraction in galaxies decrease from $M_{\text{gas}}/M_{\text{halo}} \approx 0.13$ at $M_{\text{halo}} = 10^{10} M_{\odot}$ to 0.04 at $4 \times 10^{12} M_{\odot}$. The wind (CW, RVWa, RVWb) flattens the $M_{\text{gas}}/M_{\text{halo}}$ trend making it oscillatory around $(0.08 - 0.1)$ over the same M_{halo} range. The gas fractions in galaxies are lower than the cosmic baryon to DM fraction used in our simulations ($\Omega_{B,0}/\Omega_{M,0} = 0.17$). The gas mass fractions we obtain are roughly consistent with those found in massive cluster halos ($M_{500} > 10^{13} M_{\odot}$) at $z = 0$, in simulations including baryonic physics of cooling, SF and AGN feedback (Planelles et al. 2012).

The stellar fraction is largest in NW, because the SF rate is higher in the absence of wind (§3.2.1) producing more stars for the same halo mass. The wind in the other runs expel some star-forming gas out of galaxies, reducing the SF and consequently the stellar mass. $M_{\text{stellar}}/M_{\text{halo}}$ increases from $\approx (0.01 - 0.025)$ at $M_{\text{halo}} = 10^{10} M_{\odot}$ to $\approx (0.08 - 0.16)$ at $6 \times 10^{11} M_{\odot}$, at a varying rate for the different runs, and remain almost flat at higher halo masses up to $4 \times 10^{12} M_{\odot}$. NW and RVWb have the steepest increase, followed by CW,

and RVWa is the flattest. Observations also find the stellar mass fractions of low- z galaxies increasing with halo mass between $M_{\text{halo}} \sim (10^{10} - 10^{12}) M_{\odot}$ (e.g., Papastergis et al. 2012), with a comparable slope, but the absolute values in observations are ~ 10 times smaller than our simulations.

The gas and stellar fractions reveal the mass-dependence of the feedback acting on the galaxies in the different wind models. In runs NW and RVWb, more-massive halos have lower gas fraction than stars because of efficient conversion of gas to stars, and less-massive halos have more gas than stars; causing $M_{\text{gas}}/M_{\text{halo}}$ decrease with increasing M_{halo} . In the effective wind models CW and RVWa, baryons are expelled efficiently and can escape from low-mass halos, causing the gas fraction (and star fraction) to be lower than NW and RVWb. At the high-mass end, outflows are not efficient to expel gas from halos, causing a higher gas fraction compared to cases NW and RVWb. The result is a flatter $M_{\text{gas}}/M_{\text{halo}}$ fraction versus M_{halo} in the effective outflow models. However the wind feedback affects the galaxy SFR; it is efficient enough and increases the galaxy cooling time, pre-

venting the gas from turning into stars, causing the stellar fraction to be lower than NW and RVWb in massive halos.

We thus conclude that the outflow models CW and RVWa have significant impact on the gas and stellar mass functions, as well as on the mass fractions of gas and stars in halos.

3.4 Temperature-Density Phase Diagram

The temperature versus density phase diagram of all the gas at $z = 1.98$ is plotted in Fig. 7, top row, for the LB runs in 4 horizontal panels, color coded by the gas mass fraction. The larger boxsize is chosen for the two $[T - \rho]$ diagrams we present in this section, because it gives a statistics over a larger range of halos. The x -axis denotes the density contrast, $\delta = \rho_{\text{gas}}/\langle\rho_B\rangle$, which is the comoving density of gas ρ_{gas} as a fraction of the comoving mean baryon density, $\langle\rho_B\rangle = \Omega_{B,0}3H_0^2/(8\pi G)$. The vertical dashed line is the SF threshold density (n_{SF} , §2.1) above which a fixed effective equation of state is imposed on the gas in the multiphase SF model (SH03, Wiersma et al. 2009). The hot-phase temperature is shown for the multiphase gas particles, which forms the constant-slope straight line above n_{SF} in the top-right portion of each run. In the NW run (top-left panel), all the gas denser than n_{SF} follows the equation of state, and there is no cold gas at those high densities.

In the runs with wind, a fraction of the gas denser than n_{SF} is cooler ($< 10^4$ K) than the NW case, forming a cold, dense tail in the bottom-right portion of the phase diagram. This is a consequence of the decoupling formalism of the galactic outflow implementation (§2.4). The wind particles are allowed to move away from SF regions and no longer follow the SF effective equation of state. They are however still very dense, where the cooling rate is high and cooling time short. Therefore they cool very fast, soon after being kicked into wind, and form the cold, dense extension above n_{SF} in the phase diagram. Subsequently, if the kick velocity is higher than the neighbors, the wind particles exit the dense SF region soon, moving to lower-density ($< n_{\text{SF}}$), hotter ($> 10^4 - 10^5$ K) regions. Thus in our galactic outflow models, the wind is launched from dense SF phase, and soon after that the wind goes through a cold phase.

The remaining of the phase diagram looks qualitatively similar in the 4 runs. The majority of the gas (red in Fig. 7) lies in underdense to moderately overdense ($\delta \sim 10^{-1} - 10^2$) and cool-warm ($T \sim 10^3 - 10^5$ K) phase, which is the cosmic baryons in balance between adiabatic cooling and photoionization background heating. A small fraction of gas at a higher range of overdensities ($\delta \sim 10^{-1} - 10^4$) is hot ($T \sim 10^6 - 10^8$ K), being heated by shocks during gravitational collapse. At $\delta \sim 10^2 - 10^4$, there is another cold ($T < 10^5$ K) phase which is the dense gas cooling into DM halos to form galaxies.

The gas mass fraction in the phases varies between the 4 runs, forming different patterns in the phase diagram. Runs NW and RVWb have a higher fraction of gas in the multiphase SF branch of effective equation of state. Among the wind runs, RVWb has the highest mass fraction in the cold wind phase, followed by CW and finally RVWa. This is because of the different wind kick velocity in each case; RVWb has the lowest v_w (seen in Fig. 2, §3.1) where gas is not able to escape the dense phase, while in RVWa the wind particles

are able to escape the dense phase quickly. Runs CW and RVWa have a higher fraction of underdense ($\delta < 1$), warm-hot ($T \sim 10^4 - 10^6$ K) gas, denoted by the red and yellow contours in Fig. 7, composed of gas previously ejected from dense SF regions of galaxies as strong winds.

The temperature - density phase diagram of only the CGM gas at $z = 1.98$ is plotted in Fig. 7, bottom row, for the LB runs in 4 horizontal panels. Gas particles lying inside the virial radius R_{200} (computed analytically using Eq. 7) of all the FOF halos are selected, excluding the star-forming ones (ie. particles with $\text{SFR} = 0$ are only counted). The selected CGM gas comprise of a number fraction (0.07 - 0.1) of all the gas particles in a run, and is shown in Fig. 7, color coded by the gas mass in $[T - \delta]$ bins as a fraction of the total mass plotted. The densities defining the boundaries of the CGM are denoted by the vertical dashed lines. The SF threshold density is the upper limit, above which gas forms stars and becomes part of galaxy. From Fig. 7, bottom row, we infer a lower limiting density $\delta_{\text{CGM}} = 5$ of the CGM.

The NW run (bottom-left panel) has no CGM gas denser than n_{SF} , because of imposing the $\text{SFR} = 0$ criterion for selecting CGM particles, as here all the gas denser than n_{SF} is star-forming. The runs with wind have a fraction of gas denser than n_{SF} which is not star-forming, and they are the wind-phase particles: mostly cold undergoing hydrodynamic decoupling, and a small fraction which recently received a wind kick and still in the hot multiphase branch. Noting the effect of feedback, we see that the CGM is separated into a cold $T < 10^5$ K phase and hotter gas in a more well-defined way in models CW and RVWa impacted by their effective outflows, than in NW and RVWb.

Overall, analyzing the $[T - \delta]$ plane, we can conclude that the thermal properties of the IGM remain roughly the same between the different outflow models; with the winds producing a higher fraction of underdense, warm-hot gas. Furthermore the CGM is well separated into cold and warm-hot phases by the winds.

3.5 Single Galaxy Gas Kinematics

The most-massive galaxies at $z = 2.12$ in the SB simulations are plotted in Fig. 8. The smaller boxsize is used here again for ease of visualization (like in §3.1), to clearly distinguish the outflowing gas in the plot of a massive galaxy within the box volume. Each of the 4 rows shows a unique gas property, the different wind model runs are labelled in the top-left corner of the 1st, 3rd and 4th rows. The maximum gas density location is at the center, and the panels show the projection of gas kinematics in the $[x - y]$ plane of a surrounding $(200h^{-1} \text{ kpc})^3$ volume. The total halo mass (DM + gas + stars) of the galaxies are in the range $M_{\text{halo}} = (1.4 - 1.9) \times 10^{11} M_{\odot}$. One can see the formation of a galaxy disk in runs NWt, RVWat and RVWbt of varying sizes, whereas in CWt the galaxy looks irregularly shaped in the projected plane. The galaxy disk in model RVWat is the largest in size, followed by NWt and then RVWbt. The disks in NWt and RVWbt are quite similar, with RVWbt producing a thicker disk.

In the top two rows the outflowing (radial velocity with respect to galaxy center, $v_r > 0$) particles are denoted as red, and the inflowing ($v_r < 0$) as black. The first row shows the positions of all the gas particles within the projected

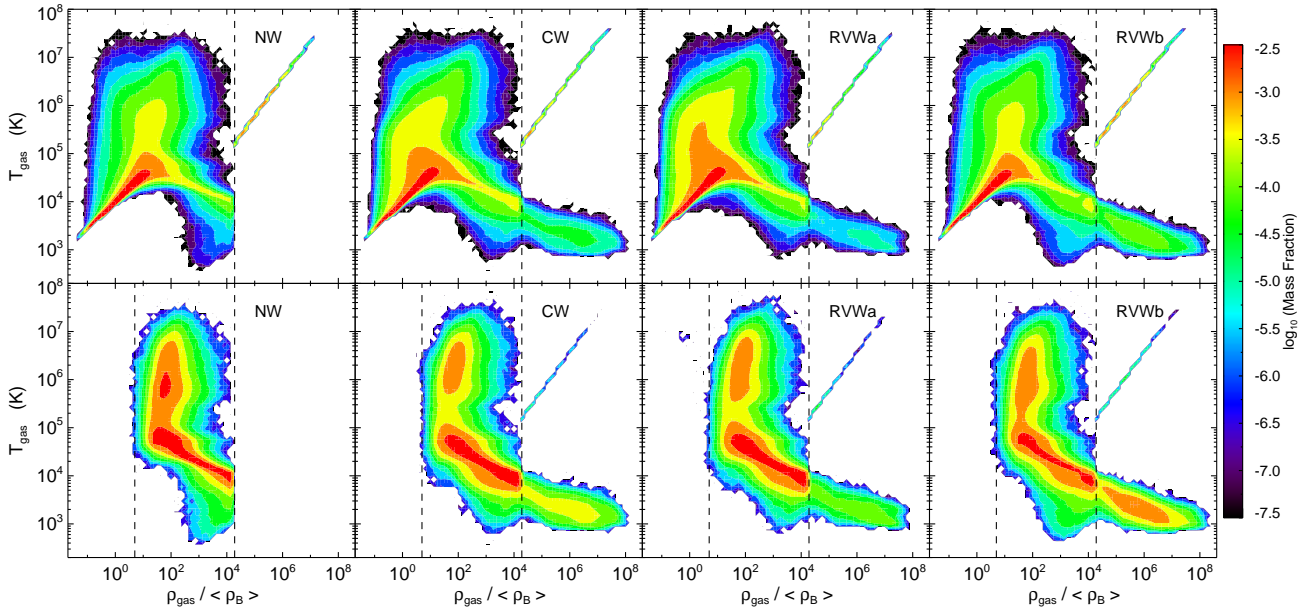


Figure 7. Temperature versus density contrast (gas comoving density as a fraction of the mean baryon density) phase diagram of all the gas (top row) and the CGM gas (bottom row), at $z = 1.98$, for the LB runs with name labeled in each panel. The gas representing the CGM shown at the bottom is selected by tracking particles lying inside R_{200} of all the halos and excluding the star-forming ones, which comprise of a number fraction (0.07 - 0.1) of all the gas particles shown in the corresponding top panel. The color code represents the mass fraction (in log-scale) of gas in density - temperature bins, with red showing the highest fractions going to black for the lowest. The single vertical dashed line in the top panels is the star formation threshold density (physical $n_{\text{SF}} \approx 0.1 \text{ cm}^{-3}$, §2.1) above which a fixed equation of state is imposed on the gas in the multiphase SF model. The hot-phase temperature is shown for the multiphase gas particles, which results in the constant-slope straight line above n_{SF} in the top-right portion of each panel (§3.4). The two vertical dashed lines in the bottom panels represent the bounding densities of the CGM: the star formation threshold density is the upper limit, and a lower limiting density $\delta_{\text{CGM}} = 5$ inferred from this plot.

volume, and the second row depicts the velocity vectors of 10% outflowing gas particles and 10% inflowing gas. The number fraction of outflowing (f_{out}) and inflowing (f_{in}) gas are written in the top-left corner of the second row panels. Within this $(200h^{-1} \text{ kpc})^3$ projected volume, in runs NWt, RVWat and RVWbt, about half of the gas is inflowing and the other half outflowing. While in run CWt more gas (64%) is undergoing infall than outflow (36%). This is likely because of fall-back of gas which was kicked outward at earlier epochs, but did not escape the halo potential, and is infalling back. The in/out flow fractions in run CWt are similar to the result by Shen et al. (2012) who found that in the *Eris2* zoom-in simulation, the CGM of a Milky Way-type galaxy at $z \sim 3$ has about one third of all the gas within the virial radius as outflowing. In our Fig. 8, the inflow is overplotted on the outflow in the first row depicting a prominence of black points over red at the center, and vice versa in the second row showing a prominence of red points over black; this demonstrates the mixture of gas dynamics (i.e. contains both inflow and outflow) in the central 20 – 30 kpc regions.

The outflow is not well-structured in the no-wind (NWt) and the low-velocity wind model (RVWbt) cases, some gas escaping along the direction of least resistance through a low-density void in the bottom-right half. In run CWt most of the outflowing gas lies inside $r < 50$ kpc, because here the wind kick velocity $v_w = 400 \text{ km/s}$ is not enough to drive the outflow to larger distances; the strong

gravitational potential of the halo causes the gas to fall back inward also resulting in a higher inflow fraction in this run. The radially-varying subgrid wind velocity $v_w(r)$ of Eq. 5 in run RVWat produces a well-developed gas outflow propagating perpendicular to the galaxy disk, escaping to $r > 100$ kpc from the center, seen as the red arrows along top-right and bottom-left in the 3rd panel of the 2nd row.

The third row of Fig. 8 shows the gas density contrast color coded on a log-scale from red as the highest and black as the lowest values. All the runs have a central overdense region, where SF occurs forming a galaxy disk in some cases. Wind particles are kicked from these SF regions, carrying a fraction of the central gas to larger distances. In run CWt the constant-velocity wind forms an extended halo of gas at $r \leq 50$ kpc, seen as yellow-green in the 2nd panel, which is most likely bound to the galaxy potential and not able to escape. The strong radially-varying wind in RVWat produces a more extended ($r \sim 100$ kpc) but lower-density diffuse outflow, which is likely escaping the galaxy in the 3rd panel. The low-velocity wind run RVWbt has most of the gas concentrated in the central 10 – 20 kpc.

Carbon metallicity (Z_C , defined in §2.5) is plotted in the fourth row of Fig. 8. Runs NWt and RVWbt have a larger central concentration of metals (red in the figure) originating from SF, because there is either no-wind or the wind is not effective to spread the metals around. The central metal content is smaller in runs CWt and RVWat, since winds carry the metals out from the SF regions and enrich the

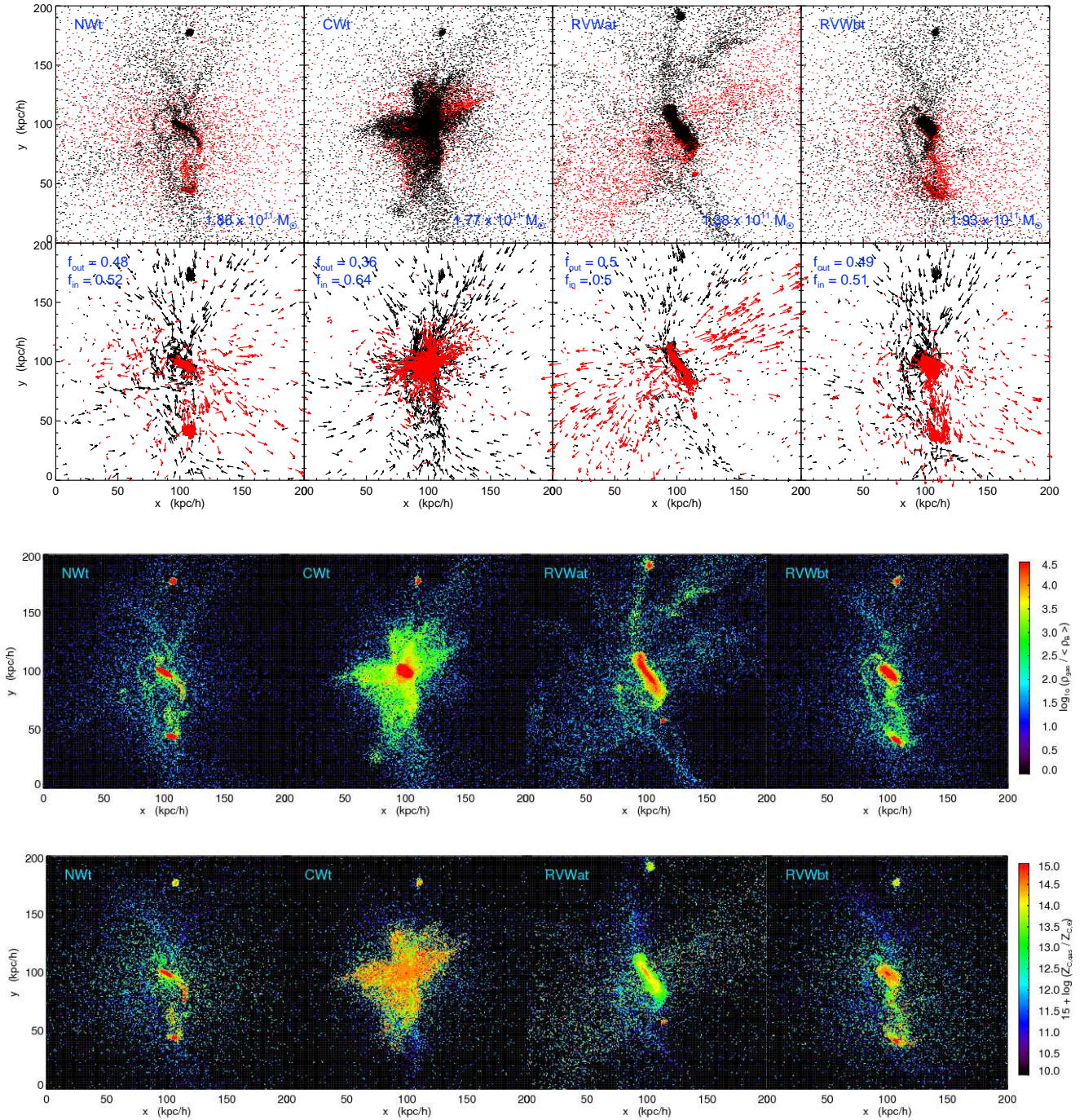


Figure 8. Projection of gas kinematics in the $[x - y]$ plane of a $(200h^{-1} \text{ kpc})^3$ volume centered around the maximum gas density location of the most-massive galaxy at redshift $z = 2.12$, in the SB simulations with different wind models (from the left): no wind, energy-driven constant-velocity, radially varying with fixed parameters, and that with halo mass dependent parameters. In the top two rows the outflowing ($v_r > 0$) particles are denoted as red, and the inflowing ($v_r < 0$) as black. First row from the top shows the positions of all the gas particles within the projected volume, and the second row depicts the velocity vectors of 10% of each component. The total halo mass of each galaxy, and the number fraction of outflowing (f_{out}) and inflowing (f_{in}) gas are written within the panels. The inflow is overplotted on the outflow in the first row, and vice versa in the second. Third row shows gas density contrast, and fourth row is carbon metallicity, color coded from red as the highest and black as the lowest values.

CGM and IGM. Consequently, in the 2nd and 3rd panels, the distribution of metals outside galaxy disk is aligned with the outflowing velocity (red arrows in the 2nd row), and two extended gas outflow regions (density contrast in the 3rd row) are present.

The large scale structure of all the runs are similar as expected from the same initial condition, though there are small-scale differences as described above arising from different wind models. There is gas inflow from bottom / bottom-right regions of the panels into the center and from top / top-right into the center, seen as black points in the 1st row, black inflowing arrows in the 2nd, overdense filaments in the 3rd, which have lower-metallicity as seen in the bottom row. These likely denote pristine gas infall along cosmological filaments that “feed” the galaxy at the center. Another common feature is the overdense gas clump 70 – 80 kpc to the top of the center, most likely an infalling sub-structure which will eventually merge with the central galaxy.

3.6 Radial Profiles Around Galaxy Centers at

$$z \sim 2$$

The radial profiles of gas properties around centers of galaxies (found by FOF group finder) at $z = 1.98$ for the LB runs are plotted in Fig. 9. The larger boxsize is chosen for all the radial profiles we present in this section, since more number of halos and more massive halos form in the larger box; it hence gives a wider statistics.

Each row of Fig. 9 shows a property as a function of comoving radius (or distance from the maximum density position considered as the galaxy center), by counting all the gas particles lying inside a distance R_{lim} from the center, in the following format. The four horizontal panels denote total (DM + gas + star) halo mass ($M_{\text{halo}}/M_{\odot}$) ranges: $10^9 - 10^{10}$ (left) with number of halos in the four plotted runs within the range $N_{\text{halo}} = 739 - 997$; $10^{10} - 10^{11}$ (second from left) having $N_{\text{halo}} = 7453 - 7906$; $10^{11} - 10^{12}$ (third from left) where $N_{\text{halo}} = 270 - 393$; $10^{12} - 10^{13}$ (right) with $N_{\text{halo}} = 10 - 12$. All the halos within each mass range are stacked, and the plotted solid curve denotes the median value in radial bins for each run labeled by the color and plotting symbol. The grey shaded area encloses the 70th percentiles above and below the median in run RVWa (red curve), showing the typical scatter at a given radius, since galaxies in general do not have spherically-symmetric properties. The vertical dashed line is the halo virial radius R_{200} in comoving coordinates (analytical expression from Eq. 7) for the following masses in the horizontal panels from left: $M_{\text{halo}}/M_{\odot} = 3 \times 10^9, 3 \times 10^{10}, 3 \times 10^{11}$ and 3×10^{12} , where the exact values are $R_{200} = 32.2, 69.4, 149.6,$ and $322.2 h^{-1}$ kpc respectively. The outer plotting radius R_{lim} is chosen to be $300 h^{-1}$ kpc for $M_{\text{halo}}/M_{\odot} = 10^9 - 10^{10}$. In the other halo mass ranges R_{lim} is scaled up according to the virial radius, making $R_{\text{lim}} = 300, 646.6, 1393.8,$ and $3001.9 h^{-1}$ kpc.

3.6.1 Density

The gas density contrast (ratio of comoving density to the comoving mean baryon density, §3.4) radial profiles are plotted in the top-most first row of Fig. 9. Within the approximate virial radius $r < R_{200}$ all the profiles are composed of

two negative-sloped functions separated by a threshold radius dependent on halo mass and wind model. At $r > R_{200}$ the density profiles tend to rise again and fall, forming a local peak. This occurs because of the presence of other smaller halos and substructures, giving rise to a local density peak. For each halo mass range a sufficiently large volume within $r \sim 10R_{200}$ is plotted to reach surrounding structures. This trend is most prominent in the lowest mass halos, and decreases at higher masses.

The inner parts $r < 10h^{-1}$ kpc of the 2 lower halo mass ranges ($10^9 - 10^{10}$ and $10^{10} - 10^{11}$, left two panels) present significant differences: CW and RVWa produce a lower density than the NW and RVWb cases, because the strong wind is able to expel gas from the star-forming regions, consequently reducing the central gas density by 10 – 30 times. The trend is almost reversed in the outer parts ($r > R_{200}$): CW, RVWa and RVWb has a somewhat higher density than NW, because of accumulation of gas expelled by wind.

The differences are smaller in the two higher halo mass ranges ($10^{11} - 10^{12}$ and $10^{12} - 10^{13}$, right two panels), because the wind, not being dependent on halo mass in runs CW and RVWa, is less effective in ejecting gas out of massive galaxies. CW produces slightly higher density (by 2 – 3 times) than RVWa in the inner $r < 10h^{-1}$ kpc, while outside this distance they are quite similar. Comparing our density radial profiles in the halo mass range $10^{12} - 10^{13}$ (top-right panel in Fig. 9), with that of Hummels et al. (2012) Fig. 5, we find qualitative agreements; however our density profiles are steeper.

3.6.2 Temperature

The temperature radial profiles are presented in the second row of Fig. 9, where the hot-phase temperature has been used for those gas particles which are multiphase (star-forming). In the inner parts $r \leq 10h^{-1}$ kpc of the galaxies, the T -profiles follow the negative-sloped density-profiles (first row of Fig. 9), for all the runs in the left 3 panels, and run NW in the right panel. This represents the dense gas near galaxy center undergoing SF, and having a high temperature ($\sim 10^5 - 10^7$ K) as a result of following the SF effective equation of state (§3.4). In the wind runs there is also the presence of cooler ($< 10^4$ K) gas, which has recently received a wind kick and undergoes hydrodynamic decoupling (§2.4). This gas was seen as the cold, dense tail in the bottom-right portion of the $[T - \rho]$ phase diagram (Fig. 7, §3.4). Consequently, runs CW, RVWa and RVWb present a bimodal T distribution at $r \leq 10h^{-1}$ kpc in some panels, composed of hot multiphase SF and cold wind.

There is a change in T slope in the outer parts, at $r \geq 6h^{-1}$ kpc in the left 2 panels and at $r \geq (20 - 30)h^{-1}$ kpc in the right 2 panels, when the gas T increases with radius, likely because of shock heating at galaxy outskirts. Between $(10 - 300)h^{-1}$ kpc, the NW model results in the highest- T ($\sim 10^5 - 10^6$ K), followed by RVWb, then RVWa and CW. Our temperature profiles show a bump at 200 – 300 kpc, which is at a larger- r than the peak of Hummels et al. (2012).

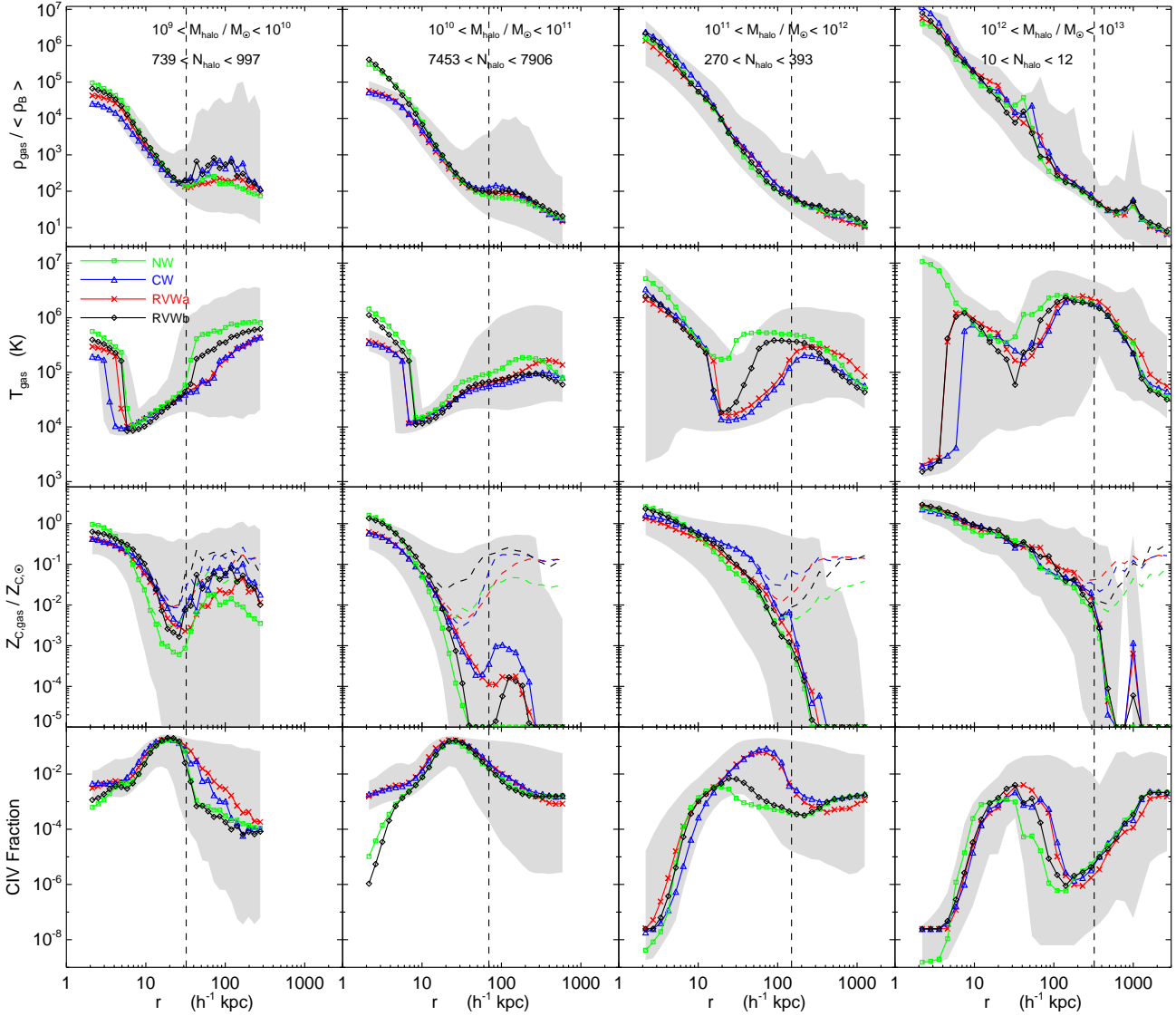


Figure 9. Radial gas profiles of galaxies found by FOF group finder at $z = 1.98$. Each row shows a gas property (described later) as a function of comoving radius (or distance from the position of maximum density considered as the galaxy center), for four total (DM + gas + star) halo mass ($M_{\text{halo}}/M_{\odot}$) ranges in the 4 horizontal panels: $10^9 - 10^{10}$ (left), $10^{10} - 10^{11}$ (second from left), $10^{11} - 10^{12}$ (third from left), and $10^{12} - 10^{13}$ (right). All the halos within each mass range (the number mentioned in the top row panels) are stacked over for each run, and the plotted curve denotes the median value in a radial bin. The grey shaded area enclose the 70th percentiles above and below the median in run RVWa (red curve), showing the typical radial scatter. The vertical dashed line is the analytical expression for the halo virial radius R_{200} in comoving coordinates (from Eq. 7), for $M_{\text{halo}}/M_{\odot} = 3 \times 10^9$, 3×10^{10} , 3×10^{11} , and 3×10^{12} in the panels from left respectively in each row. First (top-most) row is the gas density contrast. Second row is gas temperature, and hot-phase temperature is shown for the multiphase gas particles (§3.6.2). Third row is carbon metallicity, showing the ratio of carbon mass fraction in gas to that of the Sun ($Z_{C,\odot} = 0.002177$). The dashed curves in the third row represent median- Z_C for the enriched particles only in each radial bin, i.e. not counting particles with zero- Z_C (§3.6.3). Fourth row is the fraction of CIV (triply ionized carbon) in the gas (computed from simulation redshift, gas density, temperature and assuming a photoionizing background using CLOUDY ionization tables).

3.6.3 Carbon Metallicity

Radial profiles of carbon metallicity are plotted in the third row of Fig. 9, showing the ratio of carbon mass fraction in the gas to that of the Sun. The solid curve medians and percentile values are computed considering all (both enriched and non-enriched) gas particles in radial bins. The dashed curves represent median- Z_C for the enriched particles only,

i.e. those having $Z_C > 0$, without counting particles with $Z_C = 0$.

We also checked the gas fraction (by particle number) which has $Z_C > 0$. All the gas is enriched inside a limiting radius, which is $\sim 7, 10, 40,$ and $120 h^{-1}$ kpc in the panels from left, defining the size of the central SF region or the sites of metal generation. The enriched fraction decreases outside the limiting radius, with a trend depending on halo

mass and wind model: it reduces to $(0.5 - 0.8)$ at R_{200} and $(0.45 - 0.7)$ at $300 h^{-1}$ kpc. Runs CW and RVWa enrich a higher (up to 1.4 times) fraction of gas than NW and RVWb.

The dashed median Z_C in Fig. 9, third row is indistinguishable from the solid median Z_C in the inner parts, since most of the gas is enriched. While at large r the dashed median Z_C is higher, because the contribution of the non-enriched ($Z_C = 0$) particles reduces the solid median Z_C , as can be seen in all the four panels. Especially in the second and third panels the enriched median Z_C 's are 100 – 5000 times higher than the total median Z_C 's.

Some features of Z_C are similar to the gas density profiles (§3.6.1), because metals are produced during SF which occurs in dense regions. At $r < (0.4 - 0.6)R_{200}$ all the profiles show decreasing Z_C going outward from center, with varying r -dependent negative slopes, which we later fit by a second order polynomial. The Z_C profiles start to rise again from $r \geq (0.4 - 0.6)R_{200}$ and fall at larger r , forming a local peak at $r > R_{200}$. Such a trend is visible in the left two and right-most panels for both solid and dashed curves, and in the other panels for the dashed curves only. It occurs because of a combination of reasons: the presence of surrounding substructures where more metals are produced in-situ by ongoing SF, and the spreading of metals by wind from the central SF regions into the CGM. These simulation results are consistent with observations which show breaks (changes of slope) in the radial metallicity profiles, and/or rising metallicity gradients in the outer regions of galaxies (e.g., Scarano & Lepine 2012).

In the inner $r < (5 - 7)h^{-1}$ kpc CW and RVWa profiles have a lower Z_C than NW and RVWb, because wind suppresses central SF and transports some metal out. The trend reverses in the outer $r > (5 - 7)h^{-1}$ kpc: CW, RVWa and RVWb produce a metallicity about 20 – 30 times higher than NW, because of accumulation of metal-enriched gas expelled by wind. The differences are most prominent in the lower halo mass ranges ($10^9 - 10^{10}$ and $10^{10} - 10^{11}$, left two panels), and decreases at higher masses. Massive halos of $10^{11} - 10^{12}$ (third from left) still show significantly different profiles at large- r , while the profiles of the four wind models in the most-massive halos (right) are very similar.

Model RVWb produces noteworthy changes in the Z_C profile compared to NW: metallicity in the central part is slightly lower in RVWb reaching about half of NW, but starts to become larger at $r > 5h^{-1}$ kpc up to 10 times higher than NW. This shows that the wind in RVWb, though least effective in other aspects, is substantially effective in transporting metals away from SF regions into lower-density surroundings.

We perform polynomial fits to the Z_C radial profiles of runs NW and RVWa, within certain radial limits, for the 4 halo mass ranges plotted in Fig. 9. The median Z_C (solid curves) versus r data are fitted with a second order polynomial of the form, $\log(Z_C/Z_{C,\odot}) = A + B(\log r) + C(\log r)^2$, and the resulting fit coefficients are listed in Table A1. The results for $M_{\text{halo}} = (10^{10} - 10^{11})M_{\odot}$ fitted between $r = (1 - 40)h^{-1}$ kpc are:

$$\begin{aligned} \log\left(\frac{Z_C}{Z_{C,\odot}}\right) &= -0.209 + 2.23(\log r) - 3.32(\log r)^2 \quad \text{NW}, \\ &= -0.180 + 0.487(\log r) - 1.54(\log r)^2 \quad \text{RVWa}. \end{aligned}$$

We infer from Fig. 9, third row that the CGM gas at galactocentric distances close to and beyond R_{200} , within $r \sim (30 - 300)h^{-1}$ kpc comoving, around galaxies of masses $M_{\text{halo}}/M_{\odot} = 10^9 - 10^{11}$, can give the best Z_C observational diagnostic to distinguish between different galactic outflow models. Our metallicity dashed curves (enriched-particle only median, which is analogous to mass-weighted metallicity) are comparable to that of Hummels et al. (2012).

3.6.4 CIV Fraction

We compute the fraction of triply ionized carbon, CIV, of the gas particles in post-processing using photoionization tables derived from CLOUDY (last described by Ferland et al. 1998). The relevant quantities used are redshift, gas density and temperature from simulation snapshot, and an ionizing background from the HM05 tables (Haardt & Madau 2001), as included in version 07.02.00 of CLOUDY.

Fourth (bottom) row of Fig. 9 shows the radial profiles of the gas CIV fraction, f_{CIV} . There are varying positive slopes at small- r where f_{CIV} increases with radius. f_{CIV} attains a peak at an intermediate- r , which occurs at $(20 - 60)h^{-1}$ kpc depending on halo mass and wind model. Further out f_{CIV} decreases from its peak at larger- r , and have a negative slope up to $300h^{-1}$ kpc.

In the left two panels, runs CW and RVWa produce higher f_{CIV} than NW and RVWb; the differences are significant at $r \leq 7h^{-1}$ kpc reaching $10^2 - 10^4$ times, very small at larger r up to the peak of f_{CIV} , and increases again to 10 – 70 times at $r > 20h^{-1}$ kpc. The small- r positive-sloped regions in the right two panels show small differences: in the third RVWa has higher f_{CIV} than NW and RVWb, which are in turn higher than CW; whereas in the fourth (right) NW has higher f_{CIV} than CW, RVWa and RVWb. In the third panel f_{CIV} in runs CW and RVWa reaches a ~ 50 times higher peak at a larger- r than runs NW and RVWb. The large- r negative-sloped regions shows the same trends as the left 2 panels, runs CW and RVWa producing higher f_{CIV} than NW and RVWb.

We perform polynomial fits to the f_{CIV} median radial profiles, in a similar way as in §3.6.3, but with 2 first-order polynomials of the form: $\log f_{\text{CIV}} = A + B(\log r)$, within 2 radial limits. The resulting fit coefficients are listed in Table A2. The polynomials for $M_{\text{halo}} = (10^{10} - 10^{11})M_{\odot}$, fitted between $r = (1 - 6)h^{-1}$ kpc are:

$$\begin{aligned} \log f_{\text{CIV}} &= -6.58 + 5.18(\log r) \quad \text{NW}, \\ &= -3.11 + 1.01(\log r) \quad \text{RVWa}; \end{aligned} \quad (12)$$

and fitted within $r = (6 - 20)h^{-1}$ kpc are:

$$\begin{aligned} \log f_{\text{CIV}} &= -5.95 + 3.90(\log r) \quad \text{NW}, \\ &= -5.43 + 3.67(\log r) \quad \text{RVWa}. \end{aligned} \quad (13)$$

The overall behavior of f_{CIV} arises from the combined effects of density and temperature radial dependence of the gas (from first and second rows in Fig. 9) in the ionization tables, with the major role played by the temperature.

As a prediction for CIV fraction observations, we infer from Fig. 9, bottom row that the inner gas at galactocentric distances $r < (4 - 5)h^{-1}$ kpc comoving, around galaxies of masses $M_{\text{halo}}/M_{\odot} = 10^{10} - 10^{11}$, can most-effectively distinguish between strong-wind and no-wind cases.

3.7 Metallicity-Density Relation

The carbon metallicity as a function of gas density contrast is plotted in Fig. 10, at $z = 1.98$ in the top row, for the LB runs labeled by the color and plotting symbol. The larger boxsize is selected again for increased statistics, since more number of halos and more massive halos form in it. Gas particles in three temperature bins are shown: $10^4 - 10^5$ K in the top-left panel, $10^5 - 10^7$ K in the top-middle, and all the gas in the top-right. The solid curves denote the median Z_C in δ -bins for each run. The grey shaded area enclose the 70th percentiles above and below the median in run RVWa (red curve), showing the scatter at a given density. Following a format similar to Fig. 9, the solid curve medians and percentiles are computed considering all (both enriched and non-enriched) gas particles, while the dashed curves represent median- Z_C for the enriched particles only i.e. those having $Z_C > 0$. Note that if $\geq 50\%$ of the particles are not enriched, then the solid median would be zero.

The dashed median Z_C in Fig. 10, top row, coincide with the solid median Z_C at high densities, $\delta \geq 10^3 - 10^4$, because most of the dense gas is star forming, generating metals and hence enriched. While at $\delta < 10^3$ the dashed median Z_C 's are several orders of magnitude higher than the solid ones (most clear in the top-left and top-right panels), implying that most or all of the low-density and underdense gas is not enriched.

As an exception, the underdense gas having $0.1 \leq \delta \leq 2$ in the warm-hot $10^5 - 10^7$ K phase (top-middle panel) is significantly enriched by the winds in runs CW and RVWa, so that all the particles (solid curves) have a median of $Z_C/Z_{C,\odot} \sim 0.05 - 0.08$, just few times below the enriched-only dashed medians. Further trends discussed below analyzes the dashed medians wherever the solid medians are below the plotting range.

Overall the metallicity-density relation shows a negative correlation at small- δ and positive correlation at large- δ . Similar $[Z_C - \delta]$ relations were also found by Tornatore et al. (2010) for the average metallicity of the warm-hot IGM at $z = 0$. We find that the threshold density for the slope turnover depends on temperature bin and wind model, lying between $\delta = 30 - 1000$. As a special feature, run CW has a slight increase in Z_C from the smallest- δ to $\delta \sim 10$ in all the temperature bins, while run RVWa first decreases and then remains constant over the same range of densities.

The wind models produce significantly different Z_C in the low-density IGM at $\delta < 10^2 - 10^3$, with runs CW and RVWa enriching up to few 100 times higher than NW and RVWb. The metallicity induced by the four runs becomes similar at $\delta > 10^4$ in regions composed of SF gas. The warm phase of $10^4 - 10^5$ K (top-left) presents the largest differences between the wind models: CW enriches the $\delta \sim 30$ gas about 10 times more than RVWa, which is 10 times more than RVWb, which in turn is 50 times more than NW.

RVWa produces higher Z_C than CW at $\delta < 5$ (top-left panel), but for larger- δ values CW enriches more. The same trend (RVWa enriching more than CW at small δ) is visible in the other two panels (top-middle and top-right), but the resulting metallicity becomes almost comparable in RVWa and CW at larger densities.

Applying the pixel optical depth technique to quasar spectra, Schaye et al. (2003) found a positive gradient of

observed CIV metallicity with density contrast, measuring a median $[C/H] \propto 0.65 \log \delta$, in the range $\log \delta = [-0.5, 1.8]$ and $z = 1.8 - 4.1$. Comparing with our Fig. 10, dashed curves in the top row, some of the wind runs show a weak similar trend in this δ range. In all the top panels of run CW and top-middle panel of RVWa, Z_C show a weak positive correlation with δ , but with a slope ~ 4 times smaller than observed. On the other hand, runs NW and RVWb, top-left and top-right panels of RVWa, along with the all-particle solid medians of runs CW and RVWa in the top-middle panel, show a negative correlation of Z_C with δ , or almost constant Z_C . At the same time, this negative correlation is consistent with the results of Barai, Martel & Germain (2011). Studying IGM enrichment from anisotropic AGN outflows, they found that at $z \geq 2$ the underdense regions ($\delta < 1$) are enriched to higher metallicities, and the resulting $[O/H]$ decreases with increasing IGM density, a trend more prominent with increasing anisotropy of the outflows.

We perform polynomial fits to the median Z_C (solid curves) versus δ data of runs NW and RVWa, in a similar way as in §3.6.3 and §3.6.4, fitting with 2 first-order polynomials of the form: $\log(Z_C/Z_{C,\odot}) = A + B(\log \delta)$, within 2 density limits. The resulting fit coefficients are listed in Table A3, for the 3 temperature ranges plotted in Fig. 10. The polynomials in the warm-hot ($10^5 - 10^7$) K gas, fitted within $10^2 \leq \delta < 10^4$ are:

$$\begin{aligned} \log\left(\frac{Z_C}{Z_{C,\odot}}\right) &= -3.81 + 0.656(\log \delta) \text{ NW}, \\ &= -3.22 + 0.546(\log \delta) \text{ RVWa}; \end{aligned} \quad (14)$$

and fitted between $10^4 \leq \delta < 10^7$ are:

$$\begin{aligned} \log\left(\frac{Z_C}{Z_{C,\odot}}\right) &= -3.55 + 0.643(\log \delta) \text{ NW}, \\ &= -2.70 + 0.456(\log \delta) \text{ RVWa}. \end{aligned} \quad (15)$$

3.8 Redshift Evolution: Metallicity at $z \sim 4$

We investigate the redshift evolution of two metallicity correlations: Z_C versus r , and Z_C versus δ , of the LB runs.

The gas carbon abundance radial profiles of galaxies at $z = 3.98$ are plotted in Fig. 11, which is an earlier epoch than Fig. 9. The 3 panels in Fig. 11 denote 3 total halo mass ranges, $M_{\text{halo}}/M_{\odot} = 10^9 - 10^{10}$ (left panel) with number of halos in the 4 plotted runs between $N_{\text{halo}} = 800 - 1034$, $10^{10} - 10^{11}$ (middle) having $N_{\text{halo}} = 4921 - 5336$, and $10^{11} - 10^{12}$ (right) where $N_{\text{halo}} = 62 - 100$. Because of the earlier time, here no halo has grown to the highest bin mass of the previous radial profile plots at $z = 1.98$ (§3.6).

We see that several of the median Z_C versus r correlations are similar between $z = 3.98$ and $z = 1.98$, only the absolute metallicity values are lower at the earlier epoch. All the runs at $z = 3.98$ have Z_C decreasing with r at $r \leq (0.5 - 2)R_{200}$, with r -dependent negative slopes. The trend of Z_C profiles rising again at larger r values (because of in-situ metal generation in surrounding structures and spreading of metals by wind from the central SF regions) is weaker at $z = 3.98$; it is only visible for the dashed curves in all the panels and few solid curves in the left panel.

The differences between the wind models are smaller at $z = 3.98$ than $z = 1.98$, however there are signatures

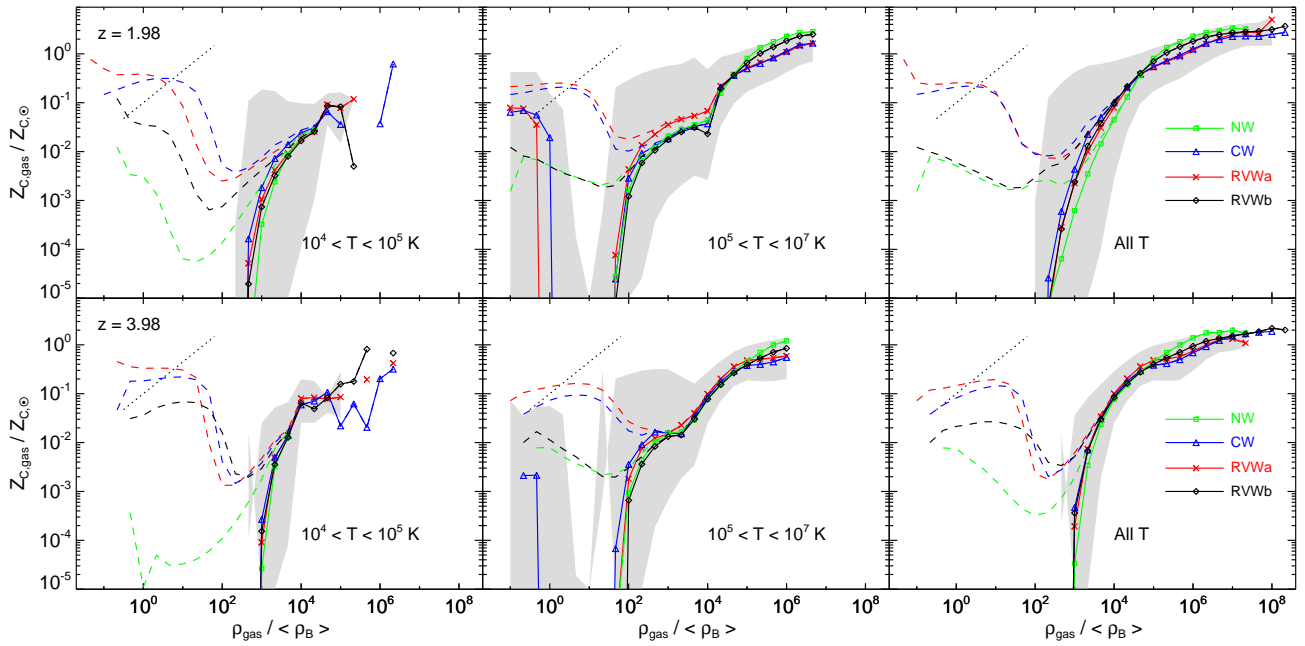


Figure 10. Carbon metallicity versus density contrast of gas at $z = 1.98$ (top row, described in §3.7), and at an earlier epoch $z = 3.98$ (bottom row, discussed in §3.8), for the LB runs labeled by the color and plotting symbol. Gas in three temperature ranges are shown: $10^4 - 10^5$ K (left panels), $10^5 - 10^7$ K (middle), and all the gas (right). The plotted solid curves denote the median value in each density bin. The grey shaded area encloses the 70th percentiles above and below the median in run RVWa (red curve), showing the typical scatter. These medians and percentiles are computed using all (both enriched and non-enriched) gas particles. The dashed curves show the median- Z_C for enriched ($Z_C > 0$) particles only in density bins. The black dotted line in each panel shows the δ -range and $[Z_C - \delta]$ slope obtained from observations by Schaye et al. (2003).

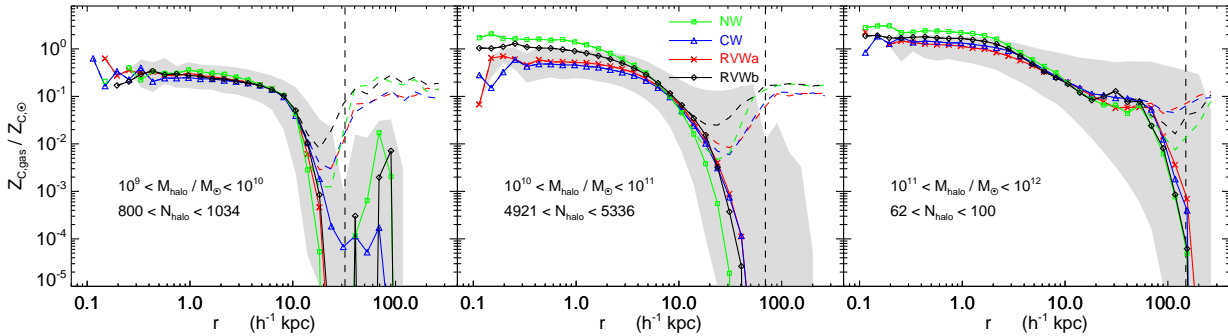


Figure 11. Gas carbon metallicity radial profile of galaxies at $z = 3.98$, an earlier epoch than in Fig. 9, third row, in a similar format. It shows the ratio of carbon mass fraction in gas to that of the Sun, as a function of comoving radius, for 3 halo mass ranges. The dashed curves represent median Z_C values for the enriched particles only in each radial bin. See §3.8.

of suppression of central SF by the impact of winds, which transport metals out and accumulate them in the CGM. Analyzing the solid curves in the middle and right panels, runs CW and RVWa have few times lower Z_C than NW and RVWb in the inner $r < (5 - 7)h^{-1}$ kpc. The trend reverses in the outer $r > (5 - 7)h^{-1}$ kpc; CW, RVWa and RVWb have few times higher metallicity than NW. The enriched-only dashed curves show a feature different from their solid counterparts in the left and middle panels, for large r values, where they detach from the solid curves and increases with r ; Z_C in runs NW and RVWb are $\sim 2 - 3$ times higher than CW and RVWa.

The bottom row of Fig. 10 shows the gas carbon metallicity versus density contrast at $z = 3.98$, for 3 temperature ranges, following the top row. Analogous to $[Z_C - r]$, several of the median Z_C versus δ correlations at $z = 3.98$ are similar to those at $z = 1.98$, with the absolute metallicity values being lower at earlier times. The differences between the wind models are smaller at $z = 3.98$ than $z = 1.98$.

The underdense gas with $0.1 \leq \delta \leq 0.8$ in the warm-hot $10^5 - 10^7$ K phase (bottom-middle panel) is already enriched by the winds in run CW, making the all-particle (solid curve) median $Z_C/Z_{C,\odot} \sim 0.002$ at $z = 3.98$, which is 40 times lower than at $z = 1.98$. However, the enrichment

at similar δ values caused by the winds of model RVWa at $z = 3.98$ is substantially lower than that of CW by 1000 times or more.

Further trends at $z = 3.98$ discussed below analyze the dashed medians wherever the solid medians are below the plotting range. Starting from the lowest- δ , the metallicity-density in all the outflow runs (except RVWb in the bottom-middle panel) show a shallow positive correlation at $\delta \leq 30$. At $z = 1.98$, such a feature is only present in run CW. This positive-sloped $[Z_C - \delta]$ relation that we obtain at $z = 3.98$ in the wind models is consistent with observations by Schaye et al. (2003) who found a positive gradient of CIV metallicity at similar overdensities.

4 SUMMARY AND CONCLUSION

We explore new models of galactic winds performing hydrodynamic simulations using the TreePM-SPH code GADGET-3, and analyze their impact on the properties of the CGM at $z = 2 - 4$. Our outflow implementation imparts kinetic feedback, in the energy-driven formalism, where the wind velocity has a positive correlation with galactocentric radius $v_w(r)$ as seen in observations by Steidel et al. (2010). We further investigate a halo mass dependent parametrization of the radially-varying wind, following observations by Martin (2005). The simulations include additional subgrid physics: metal-dependent radiative cooling and heating in the presence of photoionizing background radiation; star formation; stellar evolution and self-consistent chemical enrichment using a fixed stellar IMF.

The implementation of the new wind models in the code involves finding the distance of gas particles from their host galaxy center. We identify galaxies by running a FOF group finder on-the-fly within a simulation at intervals of 1.001 times the scale factor, and find stellar groups of at least 32 particles, by linking over stars as the primary particle type, using a linking length 3 times smaller than that for obtaining DM halos. The location of the member gas particle with maximum density is considered as the galaxy center. Multiphase gas particles undergoing SF are stochastically selected and kicked into wind by giving their speed a one-time v_w boost in a direction perpendicular to the galaxy disk. Wind particles are also temporarily decoupled from hydrodynamical interactions.

We simulate two different cosmological volumes (in order to increase the statistics) a smaller box of $(5h^{-1} \text{ Mpc})^3$ comoving with 2×128^3 DM and gas particles, and a larger box of $(25h^{-1} \text{ Mpc})^3$ with 2×320^3 particles; using the flat Λ CDM concordance model. For each volume, we perform 4 runs investigating different galactic wind models:

NW: no wind;
 CW: energy-driven wind with constant $v_w = 400$ km/s;
 RVWa: radially varying wind with fixed parameters;
 RVWb: RVW with parameters dependent on halo mass.

The main analyses of our simulations reflect the following processes: the outflows expel gas away from the star-forming galaxies and suppress the SF; the gas is also metal-enriched; thus winds carry metals out and accumulate them in the CGM and IGM, enriching these lower density regions with metals. Our results are summarized below.

- *Outflow speed.*

The outflow gas velocity magnitude as a function of galactocentric distance of multiple wind-phase gas particles, obtained in our simulations, follows the given input subgrid wind speed, constant or varying with radius, in agreement with observations.

- *Star formation rate.*

Galactic wind feedback quenches SF at $z < 8$. In the $(25h^{-1} \text{ Mpc})^3$ runs at $z \sim 2$, the global SFRD is 4 times smaller in RVWa and 2 times smaller in CW than NW. At $z \leq 5$ RVWa causes a greater suppression than CW, and produces 2 – 4 times lower SFRD than CW at $z = 2$. The SFRD at $z \sim 4.5 - 10$ is systematically (up to 2 – 10 times) higher in the simulations, compared to observations. At later epochs $z \sim 2 - 4.5$, most of the observations (e.g., Cucciati et al. 2012) lie within the ranges of SFRD produced by the different wind models.

The sSFR versus galaxy stellar mass at $z \sim 2$ present reasonably good agreement with observations, the models reproducing the observed main sequence (e.g., Daddi et al. 2007) for star forming galaxies.

- *Gas and stellar mass functions and mass fractions.*

The gas mass function of galaxies in the $(25h^{-1} \text{ Mpc})^3$ runs at $z = 2.23$ has the same slope between $M_{\text{gas}} \sim (10^9 - 10^{11})M_{\odot}$, but in CW and RVWa is shifted leftward with respect to NW and RVWb by $(2 - 3)M_{\odot}$; because winds expel gas, causing a smaller number of objects with high gas masses. Runs CW and RVWa produce a steeper stellar mass function than NW and RVWb. There is a small excess of galaxies in RVWa compared to CW between $M_{\text{stellar}} = (2 \times 10^8 - 10^9)M_{\odot}$. Our model RVWa provide a reasonably good match to the observational data of the stellar mass function at $2 \leq z < 3$ (e.g., Marchesini et al. 2009), over $M_{\text{stellar}} = (8 \times 10^9 - 10^{11})M_{\odot}$.

In run NW the gas mass fraction decreases monotonically with halo mass; outflows (runs CW, RVWa, RVWb) flatten the $M_{\text{gas}}/M_{\text{halo}}$ trend making it oscillatory. The stellar mass fraction in galaxies is the largest in run NW, and increases with M_{halo} , such that NW and RVWb have the steepest increase, followed by CW, and RVWa is the flattest.

- *Thermal state of the gas.*

The $[T - \rho]$ phase diagram shows that the outflow, soon after leaving the dense SF phase, goes through a cold ($< 10^4$ K) phase, due to the hydrodynamic decoupling. The thermal properties of the IGM look qualitatively similar in the 4 runs. Model RVWa has a higher fraction of underdense to slightly overdense ($\delta \sim 0.1 - 10$), warm-hot ($T \sim 10^4 - 10^6$ K) gas, than CW; both of them are significantly higher than NW and RVWb.

- *Gas kinematics.*

Projection of gas kinematics around the center of a galaxy of total halo mass $M_{\text{halo}} \sim 2 \times 10^{11}M_{\odot}$ at $z = 2.12$, shows that for NW and RVWb the gas outflows along the direction of least resistance of a low-density void. Run CW has most of the outflow inside $r \leq 50$ kpc forming a metal-enriched gas sphere, $v_w = 400$ km/s not being enough to drive the wind to larger distances. The $v_w(r)$ in run RVWa produces an extended diffuse enriched gas outflow propagating perpendicular to the galaxy disk (as expected from the model input), escaping to $r > 100$ kpc. The formation of a galaxy disk is visible in runs NW, RVWa and RVWb, where inside the $(200h^{-1} \text{ kpc})^3$ projection volume about half of the gas is inflowing and the other half outflowing. Whereas the CW

galaxy looks irregularly shaped, and more gas (64%) is undergoing infall than outflow (36%). The galaxy disk in run RVWa is the largest in size and further investigations are needed to check if $v_w(r)$ can produce realistic disk galaxies.

- *Radial profiles.*

The radial profiles of gas properties around galaxy centers at $z = 1.98$ show most prominent differences between the models for lower halo masses ($M_{\text{halo}}/M_{\odot} = 10^9 - 10^{10}$ and $10^{10} - 10^{11}$), and almost uniform results at higher masses. The density and carbon metallicity profiles often form a local peak at $r > R_{200}$ of galaxies, because of the presence of smaller halos and surrounding substructures where more metals are produced by in-situ SF, and the spreading of metals by wind.

- *Gas density profile.* Runs CW and RVWa have a lower density in the inner $r \leq 10h^{-1}$ kpc, by 10 – 30 times, than the NW and RVWb cases. While in the outer $r > R_{200}$, CW, RVWa and RVWb show a higher density than NW.

- *Temperature profile.* The wind runs CW, RVWa and RVWb present a bimodal temperature distribution at $r \leq 10h^{-1}$ kpc, composed of hot multiphase star forming gas and cold winds. Between $(10 - 300)h^{-1}$ kpc, the NW model cause the highest- T ($\sim 10^5 - 10^6$ K), followed by RVWb, then RVWa and CW.

- *Carbon metallicity profile.* Runs CW and RVWa have a lower Z_C than NW and RVWb in the inner $r < (5 - 7)h^{-1}$ kpc, while in the outer parts runs CW, RVWa and RVWb produces higher Z_C by 20 – 30 times than NW. Metallicity in RVWb becomes larger than in NW at $r > 5h^{-1}$ kpc and up to 10 times higher at $r \geq R_{200}$. We perform second order polynomial fits to Z_C versus r , whose coefficients are listed in Table A1.

The carbon enriched ($Z_C > 0$) gas fraction is 1 in the inner regions of galaxies; it reduces to (0.5 – 0.8) at R_{200} and to (0.45 – 0.7) at $300 h^{-1}$ kpc. Runs CW and RVWa enrich a higher (up to 1.4 times) fraction of gas than NW and RVWb.

- *CIV fraction around galaxies.* CIV fraction profiles have varying positive and negative slopes at different r , attaining a peak between $(20 - 60)h^{-1}$ kpc. Runs CW and RVWa produces higher f_{CIV} than NW and RVWb. We fit the f_{CIV} radial profiles with 2 first-order polynomials, and list the coefficients in Table A2. The results for $M_{\text{halo}} = (10^{10} - 10^{11})M_{\odot}$, fitted between $r = (1 - 6)h^{-1}$ kpc show the largest difference: $f_{\text{CIV}} \propto r^6$ for NW, and $f_{\text{CIV}} \propto r^1$ for RVWa.

- *Observational Predictions.* Inferred from our simulations, we predict that Z_C observations of the CGM gas at galactocentric distances in the range $r \sim (30 - 300)h^{-1}$ kpc comoving, around galaxies of $M_{\text{halo}} = (10^9 - 10^{11})M_{\odot}$, can best distinguish between different galactic outflow scenarios. And CIV fraction observations of the inner gas in the range $r < (4 - 5)h^{-1}$ kpc comoving, around galaxies of $M_{\text{halo}} = (10^{10} - 10^{11})M_{\odot}$, can most-effectively distinguish between strong-wind and no-wind cases.

- *Metallicity as a function of density.*

The underdense $\delta = 0.1 - 2$ warm-hot $10^5 - 10^7$ K phase is significantly enriched by the winds in runs CW and RVWa, so that the all-particles median is $Z_C/Z_{C,\odot} \sim 0.02 - 0.08$. Z_C versus δ at $z = 1.98$ shows a negative correlation at small- δ ,

and positive correlation at large- δ . The only exception is run CW where Z_C has a small increase between $\delta \sim 0.1 - 10$, while Z_C in RVWa first decreases and then remains flat. The low-density IGM with $\delta < 10^2 - 10^3$ is significantly enriched in runs CW and RVWa, up to few 100 times more than NW and RVWb. In the warm $10^4 - 10^5$ K phase, CW enriches the $\delta \sim 30$ IGM 10 times more than RVWa, which enriches 10 times more than RVWb, which in turn enriches 50 times more than NW.

We perform 2 first-order polynomial fits to the $[Z_C - \delta]$ correlation, whose coefficients are listed in Table A3. As an example, for the warm-hot ($10^5 - 10^7$) K gas, the fits within $10^2 \leq \delta < 10^4$ are: $Z_C \propto \delta^{0.656}$ for NW, and $Z_C \propto \delta^{0.546}$ for RVWa.

- *Redshift evolution.*

Several of the $[Z_C - r]$ and $[Z_C - \delta]$ correlations at $z = 3.98$ are similar to those at $z = 1.98$, with lower metallicity values and smaller differences between the wind models at the earlier epoch. The trend of Z_C radial profiles rising again at large- r is almost absent at $z = 3.98$. For $M_{\text{halo}}/M_{\odot} = 10^9 - 10^{10}$ and $10^{10} - 10^{11}$, the enriched-only median Z_C in runs NW and RVWb at large- r are 2 – 3 times higher than in CW and RVWa.

The $z = 3.98$ underdense $\delta = 0.1 - 0.8$ warm-hot $10^5 - 10^7$ K gas is enriched by the winds in run CW (but not in RVWa) making the all-particle median $Z_C/Z_{C,\odot} \sim 0.002$, which is 40 times lower than at $z = 1.98$. The $[Z_C - \delta]$ relation at $z = 3.98$ in all the wind runs (except RVWb in the warm-hot phase) shows a shallow positive correlation over $\delta \sim 0.1 - 30$, consistent with observations (Schaye et al. 2003).

In summary, we have found that the wind model with the radially varying velocity dependent on halo mass (RVWb) is the least effective in modifying IGM related properties, with results similar to the no-wind (NW) case, except that it substantially enriches the low-density CGM.

The impact of the model RVWa, for which the velocity is increasing as a function of galactocentric distance, is instead similar to the energy-driven constant-velocity implementation CW. However, it shows interesting differences that deserve to be further investigated. RVWa causes a greater suppression of SFR than CW at $z \leq 5$, this could have implications for the galaxy downsizing scenario. RVWa also produces galactic disks larger than all the other wind models, and one can study if the radially varying outflow formalism can generate more realistic disk galaxies. Run RVWa has a higher gas fraction than run CW in the low-density ($\delta \sim 0.1 - 10$) warm-hot ($10^4 - 10^6$ K) phase of the IGM, which could shed light on the missing baryon problem.

We see different trends of Z_C versus δ between the CW and RVWa models at $\delta \leq 10$, and CW outflows generally produce a higher and earlier enrichment of some IGM phases than RVWa. To explore such IGM metal-enrichment differences, future progress in this field should include computing more observable statistics from the simulations, e.g., Lyman- α flux, simulated quasar spectra, and compare them with observations of CGM and IGM at different impact parameters from galaxies.

ACKNOWLEDGMENTS

We are grateful to Volker Springel for allowing us to use the GADGET-3 code. Calculations for this paper were partly performed on the COSMOS Consortium supercomputer within the Dirac Facility jointly funded by STFC, the Large Facilities Capital Fund of BIS and the University of Cambridge, as well as the Darwin Supercomputer of the University of Cambridge High Performance Computing Service (<http://www.hpc.cam.ac.uk/>), provided by Dell Inc. using Strategic Research Infrastructure Funding from the Higher Education Funding Council for England. Simulations were also run at the CINECA Super Computer Center (CPU time assigned through an INAF-CINECA grant). We thank Olga Cucciati for sending us observational data for SFRD, and Martin Haehnelt, Giuseppe Murante for useful discussions. This work is supported by PRIN-MIUR, PRIN-INAFA 2009, INFN/PD51 grant. PB and MV are supported by the ERC Starting Grant “cosmoIGM”. ET acknowledges the Australian Research Council Centre of Excellence for All-sky Astrophysics (CAASTRO), funded by grant CE110001020. MK acknowledges a fellowship from the European Commission’s Framework Programme 7, through the Marie Curie Initial Training Network CosmoComp (PITN-GA-2009-238356).

REFERENCES

- Adelberger, K. L., Steidel, C. C., Shapley, A. E. & Pettini, M. 2003, *ApJ*, 584, 45
- Aguirre, A., Hernquist, L., Schaye, J., Weinberg, D., H., Katz, N. & Gardner, J. 2001, *ApJ*, 560, 599
- Aracil, B., Petitjean, P., Pichon, C. & Bergeron, J. 2004, *A&A*, 419, 811
- Asplund, M., Grevesse, N. & Sauval, A. J. 2005, *ASPC*, 336, 25
- Barai, P., Martel, H. & Germain, J. 2011, *ApJ*, 727, 54
- Barnes, L. A., Haehnelt, M. G., Tescari, E. & Viel, M. 2011, *MNRAS*, 416, 1723
- Benson, A. J., Bower, R. G., Frenk, C. S., Lacey, C. G., Baugh, C. M. & Cole, S. 2003, *ApJ*, 599, 38
- Bertone, S., Stoehr, F. & White, S. D. M. 2005, *MNRAS*, 359, 1201
- Bland, J. & Tully, B. 1988, *Nature*, 334, 43
- Bouche, N., Lehnert, M. D., Aguirre, A., Peroux, C. & Bergeron, J. 2007, *MNRAS*, 378, 525
- Bouche, N., Hohensee, W., Vargas, R., Kacprzak, G. G., Martin, C. L., Cooke, J. & Churchill, C. W. 2012, *MNRAS*, tmp, 3207
- Bouwens, R. J. et al. 2009, *ApJ*, 705, 936
- Bouwens, R. J. et al. 2012, *ApJ*, 754, 83
- Bower, R. G., Benson, A. J. & Crain, R. A. 2012, *MNRAS*, 422, 2816
- Brook, C. B., Gibson, B. K., Martel, H. & Kawata, D. 2005, *ApJ*, 630, 298
- Cen, R. & Ostriker, J. P. 2000, *ApJ*, 538, 83
- Chabrier, G. 2003, *PASP*, 115, 763
- Chattopadhyay, I., Sharma, M., Nath, B. B. & Ryu, D. 2012, *MNRAS*, 423, 2153
- Chevalier, R. A. & Clegg, A. W. 1985, *Nature*, 317, 44
- Choi, J.-H. & Nagamine, K. 2011, *MNRAS*, 410, 2579
- Cucciati, O. et al. 2012, *A&A*, 539, A31
- Daddi, E. et al. 2007, *ApJ*, 670, 156
- Dalla Vecchia, C. & Schaye, J. 2008, *MNRAS*, 387, 1431
- Dalla Vecchia, C. & Schaye, J. 2012, accepted in *MNRAS*, (arXiv: 1203.5667)
- Diamond-Stanic, A. M., Moustakas, J., Tremonti, C. A., Coil, A. L., Hickox, R. C., Robaina, A. R., Rudnick, G. H. & Sell, P. H. 2012, *ApJ*, 755, L26
- Dubois, Y. & Teyssier, R. 2008, *A&A*, 477, 79
- Erb, D. K., Quider, A. M., Henry, A. L. & Martin, C. L. 2012, *ApJ*, 759, 26
- Everett, J. E., Schiller, Q. G. & Zweibel, E. G. 2010, *ApJ*, 711, 13
- Fabjan, D., Borgani, S., Tornatore, L., Saro, A., Murante, G. & Dolag, K. 2010, *MNRAS*, 401, 1670
- Ferland, G. J., Korista, K. T., Verner, D. A., Ferguson, J. W., Kingdon, J. B. & Verner, E. M. 1998, *PASP*, 110, 761
- Fox, A. J., Ledoux, C., Petitjean, P. & Srianand, R. 2007, *A&A*, 473, 791
- Franx, M., Illingworth, G. D., Kelson, D. D., van Dokkum, P. G. & Tran, K.-V. 1997, *ApJ*, 486, L75
- Friedli, D. & Benz, W. 1995, *A&A*, 301, 649
- Gauthier, J.-R. & Chen, H.-W. 2012, *MNRAS*, 424, 1952
- Germain, J., Barai, P. & Martel, H. 2009, *ApJ*, 704, 1002
- Governato, F. et al. 2004, *ApJ*, 607, 688
- Governato, F., Willman, B., Mayer, L., Brooks, A., Stinson, G., Valenzuela, O., Wadsley, J. & Quinn, T. 2007, *MNRAS*, 374, 1479
- Haardt, F. & Madau, P. 2001, XXXVIth Rencontres de Moriond, XXIst Moriond Astrophysics Meeting, Editors D.M.Neumann & J.T.T.Van, 64
- Heckman, T. M., Armus, L. & Miley, G. K. 1990, *ApJS*, 74, 833
- Heckman, T. M. 2003, *RMxAC*, 17, 47
- Hummels, C., Bryan, G., Smith, B & Turk, M. 2012, arXiv: 1212.2965
- Johnson, H. E. & Axford, W. I. 1971, *ApJ*, 165, 381
- Katz, N. 1992, *ApJ*, 391, 502
- Katz, N., Weinberg, D. H. & Hernquist, L. 1996, *ApJS*, 105, 19
- Kawata, D. 2001, *ApJ*, 558, 598
- Kawata, D. & Rauch, M. 2007, *ApJ*, 663, 38
- Kay, S. T., Thomas, P. A. & Theuns, T. 2003, *MNRAS*, 343, 608
- Khalatyan, A., Cattaneo, A., Schramm, M., Gottlober, S., Steinmetz, M. & Wisotzki, L. 2008, *MNRAS*, 387, 13
- Kollmeier, J. A., Miralda-Escude, J., Cen, R. & Ostriker, J. P. 2006, *ApJ*, 638, 52
- Komatsu, E. et al. 2011, *ApJS*, 192, 18
- Larson, R. B. 1974, *MNRAS*, 169, 229
- Larson, R. B. & Dinerstein, H. L. 1975, *PASP*, 87, 911
- Lehnert, M. D. & Heckman, T. M. 1996, *ApJ*, 462, 651
- Lesgourgues, J., Viel, M., Haehnelt, M. G. & Massey, R. 2007, *JCAP*, 11, 008
- Lewis, A., Challinor, A. & Lasenby, A. 2000, *ApJ*, 538, 473
- Lundgren, B. F. et al. 2012, arXiv: 1207.7077
- Lynds, C. R. & Sandage, A. R. 1963, *ApJ*, 137, 1005
- Marchesini, D., van Dokkum, P. G., Forster Schreiber, N. M., Franx, M., Labbe, I. & Wuyts, S. 2009, *ApJ*, 701, 1765
- Marri, S. & White, S. D. M. 2003, *MNRAS*, 345, 561
- Martin, C. L. 1999, *ApJ*, 513, 156
- Martin, C. L. 2005, *ApJ*, 621, 227

- Mathews, W. G. & Baker, J. C. 1971, *ApJ*, 170, 241
- McCarthy, P. J., van Breugel, W. & Heckman, T. 1987, *AJ*, 93, 264
- McDonald, P., Seljak, U., Cen, R., Bode, P. & Ostriker, J. P. 2005, *MNRAS*, 360, 1471
- Mihos, J. C. & Hernquist, L. 1994, *ApJ*, 437, 611
- Monaghan, J. J. 1997, *JCoPh*, 136, 298
- Mori, M., Yoshii, Y., Tsujimoto, T. & Nomoto, K. 1997, *ApJ*, 478, L21
- Murante, G., Monaco, P., Giovalli, M., Borgani, S. & Diaferio, A. 2010, *MNRAS*, 405, 1491
- Murray, N., Quataert, E. & Thompson, T. A. 2005, *ApJ*, 618, 569
- Nagamine, K., Wolfe, A. M., Hernquist, L., Springel, V. 2007, *ApJ*, 660, 945
- Nath, B. B. & Silk, J. 2009, *MNRAS*, 396, L90
- Navarro, J. F. & White, S. D. M. 1993, *MNRAS*, 265, 271
- Newman, S. F. et al. 2012a, *ApJ*, 752, 111
- Newman, S. F. et al. 2012b, *arXiv: 1207.5897*
- Okamoto, T., Eke, V. R., Frenk, C. S. & Jenkins, A. 2005, *MNRAS*, 363, 1299
- Okamoto, T., Frenk, C. S., Jenkins, A. & Theuns, T. 2010, *MNRAS*, 406, 208
- Oppenheimer, B. D. & Davé, R. 2006, *MNRAS*, 373, 1265
- Oppenheimer, B. D., Davé, R. 2008, *MNRAS*, 387, 577
- Oppenheimer, B. D., Davé, R., Katz, N., Kollmeier, J. A., Weinberg, D. H., *MNRAS*, 2012, 420, 829
- Ouchi, M. et al. 2004, *ApJ*, 611, 660
- Padovani, P. & Matteucci, F. 1993, *ApJ*, 416, 26
- Papastergis, E., Cattaneo, A., Huang, S., Giovanelli, R. & Haynes, M. P. 2012, accepted in *ApJ*, (*arXiv: 1208.5229*)
- Perez-Gonzalez, P. G. et al. 2005, *ApJ*, 630, 82
- Pettini, M., Shapley, A. E., Steidel, C. C., Cuby, J.-G., Dickinson, M., Moorwood, A. F. M., Adelberger, K. L. & Gialalisco, M. 2001, *ApJ*, 554, 981
- Pettini, M., Rix, S. A., Steidel, C. C., Adelberger, K. L., Hunt, M. P. & Shapley, A. E. 2002, *ApJ*, 569, 742
- Pieri, M. M., Martel, H. & Grenon, C. 2007, *ApJ*, 658, 36
- Pinsonneault, S., Martel, H. & Pieri, M. M. 2010, *ApJ*, 725, 2087
- Piontek, F. & Steinmetz, M. 2011, *MNRAS*, 410, 2625
- Planelles, S., Borgani, S., Dolag, K., Ettori, S., Fabjan, D., Murante, G. & Tornatore, L. 2012, *arXiv: 1209.5058*
- Puchwein, E., Pfrommer, C., Springel, V., Broderick, A. E. & Chang, P. 2012, *MNRAS*, 423, 149
- Puchwein, E. & Springel, V. 2012, *arXiv:1205.2694*
- Rasera, Y. & Teyssier, R. 2006, *A&A*, 445, 1
- Reddy, N. A. & Steidel, C. C. 2009, *ApJ*, 692, 778
- Robertson, B., Yoshida, N., Springel, V. & Hernquist, L. 2004, *ApJ*, 606, 32
- Rodighiero, G. et al. 2010, *A&A*, 515, A8
- Rodighiero, G. et al. 2011, *ApJ*, 739, L40
- Rupke, D. S., Veilleux, S. & Sanders, D. B. 2005, *ApJS*, 160, 115
- Salpeter, E. E. 1955, *ApJ*, 121, 161
- Samui, S., Subramanian, K. & Srianand, R. 2010, *MNRAS*, 402, 2778
- Scannapieco, E., Ferrara, A. & Madau, P. 2002, *ApJ*, 574, 590
- Scannapieco, C., Tissera, P. B., White, S. D. M. & Springel, V. 2006, *MNRAS*, 371, 1125
- Scarano, S. Jr. & Lepine, J. R. D. 2012, accepted in *MNRAS* (*arXiv: 1209.5031*)
- Schaye, J., Aguirre, A., Kim, T.-S., Theuns, T., Rauch, M. & Sargent, W. L. W. 2003, *ApJ*, 596, 768
- Schaye, J. et al. 2010, *MNRAS*, 402, 1536
- Schiminovich, D. et al. 2005, *ApJ*, 619, L47
- Shapley, A. E., Steidel, C. C., Pettini, M. & Adelberger, K. L. 2003, *ApJ*, 588, 65
- Sharma, M., Nath, B. B. & Shchekinov, Y. 2011, *ApJ*, 736, L27
- Sharma, M. & Nath, B. B. 2012, *ApJ*, 750, 55
- Shen, S., Madau, P., Guedes, J., Mayer, L. & Prochaska, J. X. 2012, *arXiv: 1205.0270*
- Sommer-Larsen, J., Gotz, M. & Portinari, L. 2003, *ApJ*, 596, 47
- Springel, V., Yoshida, N. & White, S. D. M. 2001, *NewA*, 6, 79
- Springel, V. & Hernquist, L. 2002, *MNRAS*, 333, 649
- Springel, V. & Hernquist, L. 2003, *MNRAS*, 339, 289
- Springel, V. 2005, *MNRAS*, 364, 1105
- Steidel, C. C., Adelberger, K. L., Gialalisco, M., Dickinson, M. & Pettini, M. 1999, *ApJ*, 519, 1
- Steidel, C. C., Erb, D. K., Shapley, A. E., Pettini, M., Reddy, N., Bogosavljevic, M., Rudie, G. C. & Rakic, O. 2010, *ApJ*, 717, 289
- Steinmetz, M. & Muller, E. 1995, *MNRAS*, 276, 549
- Stinson, G. S., Dalcanton, J. J., Quinn, T., Kaufmann, T. & Wadsley, J. 2007, *ApJ*, 667, 170
- Strickland, D. K., Heckman, T. M., Weaver, K. A. & Dahlem, M. 2000, *AJ*, 120, 2965
- Strickland, D. K., Heckman, T. M., Colbert, E. J. M., Hoopes, C. G. & Weaver, K. A. 2004, *ApJ*, 606, 829
- Stringer, M. J., Bower, R. G., Cole, S., Frenk, C. S. & Theuns, T. 2012, *MNRAS*, 423, 1596
- Tescari, E., Viel, M., Tornatore, L. & Borgani, S. 2009, *MNRAS*, 397, 411
- Tescari, E., Viel, M., D'Odorico, V., Cristiani, S., Calura, F., Borgani, S. & Tornatore, L. 2011, *MNRAS*, 411, 826
- Thacker, R. J. & Couchman, H. M. P. 2000, *ApJ*, 545, 728
- Theuns, T., Viel, M., Kay, S., Schaye, J., Carswell, R. F. & Tzanavaris, P. 2002, *ApJ*, 578, L5
- Thielemann, F.-K. et al. 2003, *Nuclear Physics A*, 718, 139
- Tornatore, L., Borgani, S., Matteucci, F., Recchi, S. & Tozzi, P. 2004, *MNRAS*, 349, L19
- Tornatore, L., Borgani, S., Dolag, K. & Matteucci, F. 2007, *MNRAS*, 382, 1050
- Tornatore, L., Borgani, S., Viel, M. & Springel, V. 2010, *MNRAS*, 402, 1911
- Uhlir, M., Pfrommer, C., Sharma, M., Nath, B. B., Enblin, T. A. & Springel, V. 2012, *MNRAS*, 423, 2374
- van den Hoek, L. B. & Groenewegen, M. A. T. 1997, *A&AS*, 123, 305
- van der Burg, R. F. J., Hildebrandt, H. & Erben, T. 2010, *A&A*, 523, A74
- Veilleux, S., Cecil, G., Bland-Hawthorn, J., Tully, R. B., Filippenko, A. V. & Sargent, W. L. W. 1994, *ApJ*, 433, 48
- Veilleux, S., Cecil, G. & Bland-Hawthorn, J. 2005, *ARA&A*, 43, 769
- Viel, M., Schaye, J. & Booth, C. M. 2012, *arXiv: 1207.6567*
- Vikhlinin, A. et al. 2009, *ApJ*, 692, 1060
- Weil, M. L., Eke, V. R. & Efstathiou, G. 1998, *MNRAS*,

300, 773

Wiersma, R. P. C., Schaye, J. & Smith, B. D. 2009, MNRAS, 393, 99

Wiersma, R. P. C., Schaye, J., Theuns, T., Dalla Vecchia, C. & Tornatore, L. 2009, MNRAS, 399, 574

Woosley, S. E. & Weaver, T. A. 1995, ApJS, 101, 181

Zhang, D. & Thompson, T. A. 2012, MNRAS, 424, 1170

APPENDIX A:

Table A1. Polynomial Fit of Carbon Metallicity Radial Profile. Coefficients from fitting median Z_C versus r data with a second order polynomial of the form, $\log(Z_C/Z_{C,\odot}) = A + B(\log r) + C(\log r)^2$. Fits are calculated for 2 runs from Fig. 9, third row, at $z = 1.98$, for the 4 halo mass ranges (4 panels in the figure) within radial ranges indicated here. Columns 1, 2: Minimum and maximum halo mass indicating the range of the median Z_C result. Columns 3, 4: Minimum and maximum radius from galaxy center within which the fit is done. Column 5: Name of simulation run. Columns 6, 7, 8: Fitting coefficients A , B , C .

$M_{\text{halo,min}}$ [M_{\odot}]	$M_{\text{halo,max}}$ [M_{\odot}]	r_{min} [h^{-1} kpc]	r_{max} [h^{-1} kpc]	Run Name	Fit Coefficients				
				A	B	C			
10^9	10^{10}	1	30	NW	0.578	-0.685	-1.60		
10^9	10^{10}	1	30	RVWa	-0.519	1.08	-1.85		
10^{10}	10^{11}	1	40	NW	-0.209	2.23	-3.32		
10^{10}	10^{11}	1	40	RVWa	-0.180	0.487	-1.54		
10^{11}	10^{12}	1	300	NW	0.227	0.583	-1.03		
10^{11}	10^{12}	1	300	RVWa	-0.265	1.02	-1.03		
10^{12}	10^{13}	1	300	NW	0.373	-0.0354	-0.384		
10^{12}	10^{13}	1	300	RVWa	0.498	-0.241	-0.255		

Table A2. Polynomial Fit of CIV Fraction Radial Profile. Coefficients from fitting median f_{CIV} versus r data with two first-order polynomials of the form: $\log f_{\text{CIV}} = A_1 + B_1(\log r)$ within $[r_{1,\text{min}}, r_{1,\text{max}}]$, and $\log f_{\text{CIV}} = A_2 + B_2(\log r)$ within $[r_{2,\text{min}}, r_{2,\text{max}}]$. Fits are calculated for 2 runs from Fig. 9, fourth row, at $z = 1.98$, for the 4 halo mass ranges (4 panels in the figure). Columns 1, 2: Minimum and maximum halo mass indicating the range of the median f_{CIV} result. Column 3: Name of simulation run. Columns 4, 5: Minimum and maximum radius from galaxy center within which first fit is done. Columns 6, 7: Fitting coefficients A_1 , B_1 . Columns 8, 9: Minimum and maximum radius from galaxy center within which second fit is done. Columns 10, 11: Fitting coefficients A_2 , B_2 .

$M_{\text{halo,min}}$ [M_{\odot}]	$M_{\text{halo,max}}$ [M_{\odot}]	Run Name	$r_{1,\text{min}}$ [h^{-1} kpc]	$r_{1,\text{max}}$ [h^{-1} kpc]	Fit Coeffs-1		$r_{2,\text{min}}$ [h^{-1} kpc]	$r_{2,\text{max}}$ [h^{-1} kpc]	Fit Coeffs-2			
				A_1	B_1			A_2	B_2			
10^9	10^{10}	NW	1	6	-3.92	2.18	6	20	-5.27	3.69		
10^9	10^{10}	RVWa	1	6	-2.68	0.613	6	20	-4.54	3.13		
10^{10}	10^{11}	NW	1	6	-6.58	5.18	6	20	-5.95	3.90		
10^{10}	10^{11}	RVWa	1	6	-3.11	1.01	6	20	-5.43	3.67		
10^{11}	10^{12}	NW	2	7	-12.19	9.52	7	20	-4.87	1.96		
10^{11}	10^{12}	RVWa	2	7	-10.63	8.05	7	20	-5.94	2.90		
10^{12}	10^{13}	NW	4	10	-16.50	13.29	10	30	-3.78	0.624		
10^{12}	10^{13}	RVWa	4	10	-14.13	9.66	10	30	-7.17	3.10		

Table A3. Polynomial Fit of Carbon Metallicity-Density Contrast Relation. Coefficients from fitting median Z_C versus $\delta = \rho_{\text{gas}}/\langle\rho_B\rangle$ data with two first-order polynomials of the form: $\log(Z_C/Z_{C,\odot}) = A_1 + B_1(\log \delta)$ within $[\delta_{1,\text{min}}, \delta_{1,\text{max}}]$, and $\log(Z_C/Z_{C,\odot}) = A_2 + B_2(\log \delta)$ within $[\delta_{2,\text{min}}, \delta_{2,\text{max}}]$. Fits are calculated for 2 runs from Fig. 10 at $z = 1.98$, for the 3 given temperature ranges (3 panels in the figure). Columns 1, 2: Minimum and maximum temperature indicating the range of the median Z_C result. Column 3: Name of simulation run. Columns 4, 5: Minimum and maximum density contrast within which first fit is done. Columns 6, 7: Fitting coefficients A_1, B_1 . Columns 8, 9: Minimum and maximum density contrast within which second fit is done. Columns 10, 11: Fitting coefficients A_2, B_2 .

T_{min} [° K]	T_{max} [° K]	Run Name	$\delta_{1,\text{min}}$	$\delta_{1,\text{max}}$	Fit Coeffs-1 A_1 B_1		$\delta_{2,\text{min}}$	$\delta_{2,\text{max}}$	Fit Coeffs-2 A_2 B_2	
10^4	10^5	NW	10^3	10^5	-7.54	1.43	-	-	-	-
10^4	10^5	RVWa	10^3	10^5	-5.59	0.937	-	-	-	-
10^5	10^7	NW	10^2	10^4	-3.81	0.656	10^4	10^7	-3.55	0.643
10^5	10^7	RVWa	10^2	10^4	-3.22	0.546	10^4	10^7	-2.70	0.456
10^2	10^8	NW	10^3	10^5	-7.62	1.54	10^5	10^8	-1.20	0.247
10^2	10^8	RVWa	10^3	10^5	-5.98	1.19	10^5	10^8	-1.74	0.300